

Louisiana State University

LSU Scholarly Repository

LSU Doctoral Dissertations

Graduate School

7-6-2020

Quantum Criticality in Strongly Correlated Electron Systems

Samuel Obadiah Kellar

Louisiana State University and Agricultural and Mechanical College

Follow this and additional works at: https://repository.lsu.edu/gradschool_dissertations



Part of the [Condensed Matter Physics Commons](#), and the [Numerical Analysis and Scientific Computing Commons](#)

Recommended Citation

Kellar, Samuel Obadiah, "Quantum Criticality in Strongly Correlated Electron Systems" (2020). *LSU Doctoral Dissertations*. 5319.

https://repository.lsu.edu/gradschool_dissertations/5319

This Dissertation is brought to you for free and open access by the Graduate School at LSU Scholarly Repository. It has been accepted for inclusion in LSU Doctoral Dissertations by an authorized graduate school editor of LSU Scholarly Repository. For more information, please contact gradetd@lsu.edu.

QUANTUM CRITICALITY IN STRONGLY CORRELATED ELECTRON SYSTEMS

A Dissertation

Submitted to the Graduate Faculty of the
Louisiana State University and
Agricultural and Mechanical College
in partial fulfillment of the
requirements for the degree of
Doctor of Philosophy

in

The Department of Physics and Astronomy

by

Samuel Obadiah Kellar
B.S., Brigham Young University, 2011
August 2020

Acknowledgments

With many thanks to my family and friends who have supported me throughout this endeavor. A special thank you to my wife who stuck with me through joys and sorrows on this journey. Also to my advisor Dr. Jarrell who sacrificed much to get me to this point. I am also grateful to my parents for their kind words and encouragement and to Ka-Ming Tam who graciously has taken on the role of my advisor with the passing of Dr. Jarrell. I also thank Hartmut Kaiser who graciously guided me through our efforts in research.

Table of Contents

Acknowledgments	ii
List of Figures	v
Abstract	vi
Chapter 1: Chapter Introduction	1
1.1 High Temperature Superconducting Cuprates	2
1.2 Solving Strongly Correlated Systems	4
Chapter 2: Chapter Fermi Liquid Theory	7
2.1 Non-interacting Fermions: Fermi Gas	7
2.2 Interacting Fermions: Fermi Liquid	13
2.3 Conventional Superconductivity	22
2.4 Cuprate Superconductor	24
2.5 Quantum Critical Point	28
Chapter 3: Chapter Numerical Solutions to the Hubbard Model	32
3.1 Hubbard Model	32
3.2 Green Function	33
3.3 Dynamical Mean Field Approximation	36
3.4 Dynamical Cluster Approximation	45
Chapter 4: Chapter Non-Fermi Liquid and Quantum Critical Point	51
4.1 Findings in Two Dimensions	51
4.2 Current Work	54
Chapter 5: Chapter HPX Implementation of the Parquet Algorithm	61
5.1 Motivation	61
5.2 Parquet Formalism	62
5.3 Introduction of HPX	64
5.4 HPX Runtime System	69
5.5 Application on the Parquet Algorithm	71
5.6 Summary	71
Chapter 6: Chapter Conclusion	74
6.1 Summary	74
6.2 Network Performance	75
6.3 Importance	76
6.4 Future Work	76
References	77

Vita	83
------------	----

List of Figures

1.1	Qualitative phase diagram [1] of the hole doped cuprates.	3
2.1	Qualitative view of electrons in a Fermi sea.	8
2.2	A qualitative view of Fermi statistics at and near $0K$	11
2.3	Specific heat at different field strengths and resistivity of $CeAl_3$. . .	16
2.4	Ladder diagrams of pairing susceptibility.	23
2.5	Resistivity of $Br_2Si_2CaCu_2O_{8+x}$ at various concentrations.	25
2.6	Qualitative phase diagram of the cuprates [1].	27
3.1	A two dimensional cluster illustrating tiling of the Brillouin zone. .	46
3.2	The dynamical cluster approximation self-consistency loop.	49
4.1	Quasiparticle weight of the lowest Matsubara frequency v temperature.	52
4.2	Phase diagram of the two dimensional Hubbard model.	54
4.3	Various fillings for the quasiparticle weight of the 3D Hubbard model.	55
4.4	The monotonic decrease of the crossover temperature verses doping.	58
4.5	The spectra at different β for the filling of $N = 0.95$	59
4.6	The cluster susceptibility of the 3D Hubbard model.	60
5.1	The self-consistent loop of the parquet algorithm.	64
5.2	A diagrammatic representation of message coalescing.	67
5.3	The underlying architecture of HPX.	70
5.4	Structure of an HPX parcel.	71
5.5	The network parameters resulting in speedup of parquet simulation.	72

Abstract

The study of the Hubbard model in three dimensions contains a variety of phases dependent upon the chosen parameters. This thesis shows that there is the indication of a zero temperature phase transition at a finite doping. The Hubbard model has been used to identify a similar quantum critical point in two dimensions. The presented results continue these investigations. The system demonstrates a strange metal phase at finite temperature which cannot be described in term of the conventional Fermi liquid. While there have been extensive studies over the past three decades for such materials in two dimensions, there are few numerical studies in three dimensions. This study strives to identify the existence of the strange metal beyond two dimensions. In this work we present numerical results based on the dynamical cluster approximation to demonstrate the existence of a strange metal phase in three dimensions.

Chapter 1

Introduction

Many body physics studies the properties of systems which emerge due to the interactions between the large number of particles within said systems. Typically these studies focus on systems which are microscopic in nature. That is, systems where quantum mechanical effects determine their states. Many exotic properties of matter occur in such environments. Observed phenomena such as the Mott-Hubbard transition [2], antiferromagnetism [3], spin waves [4], and superconductivity serve to highlight only a few of the wide ranging effects which occur in such systems. The variety of interesting physics available speaks to the complexities involved with understanding many body systems. A general theory simultaneously capturing all phenomena is far beyond any current capability. This thesis chooses to focus on a small subset of these problems. Specifically a strongly correlated system where a large number of fermions interact on a lattice. The findings in this field prove to be very rich.

Strongly correlated systems concern the instances when electron-electron interactions cannot be ignored. Correlations between electrons explain the development of exciting results such as colossal magnetoresistance [5], where the resistivity of a material changes by orders of magnitude in the presence of an external magnetic field, and the fractional quantum hall effect [6] amongst others. The area of strongly correlated physics is an active one due to the abundance of phenomena many of which are poorly understood at a theoretical level. At times there are competing interactions which drive the system into different states. While such competitions increase the complexity they simultaneously offer a richer field of study.

A measure of the richness a system can be seen through the phase diagrams produced. This gives an indication of the differing interactions at play. Finding appropriate theories which capture the changing phases continues to be an endeavor of research in physics. In order to properly confirm a theory it is helpful to understand the phases which are available to a system. Experiment proves very useful in this regard as it informs the theorist of the qualities a developing theory should encapsulate.

1.1 High Temperature Superconducting Cuprates

The discovery of high temperature superconductor in 1986 is perhaps the most influential topic in modern condensed matter physics. Bednorz and Müller [7] discovered the first material whose critical superconducting temperature exceeded $30K$. This led to a flurry of research and resulted in the discovery of copper oxide superconductors whose critical temperature exceed $90K$ [8] and since have been recorded above $150K$ in a high pressure environment [9].

The existence of superconductivity above the liquid nitrogen temperature not only presents a opportunity in the various applications. It inspires many seemingly different branches of condensed matter physics theory. These include frustrated magnetism, topological excitations, doped Mott insulators, pseudo-gap phenomenon, anyon superconductivity, marginal fermi liquid, quantum critically, and many more. While not all the theories turn out to be appropriate for explaining the physics of the high temperature superconducting cuprates, the quest for understanding the mechanism has been a main driving force for many branches of condensed matter theories over the past three decades.

Today, the mechanism controlling high temperature superconductivity remains a topic of active research and much debate. Though there have been literally tens of thousands of peer reviewed articles on the subject there is still no consensus as

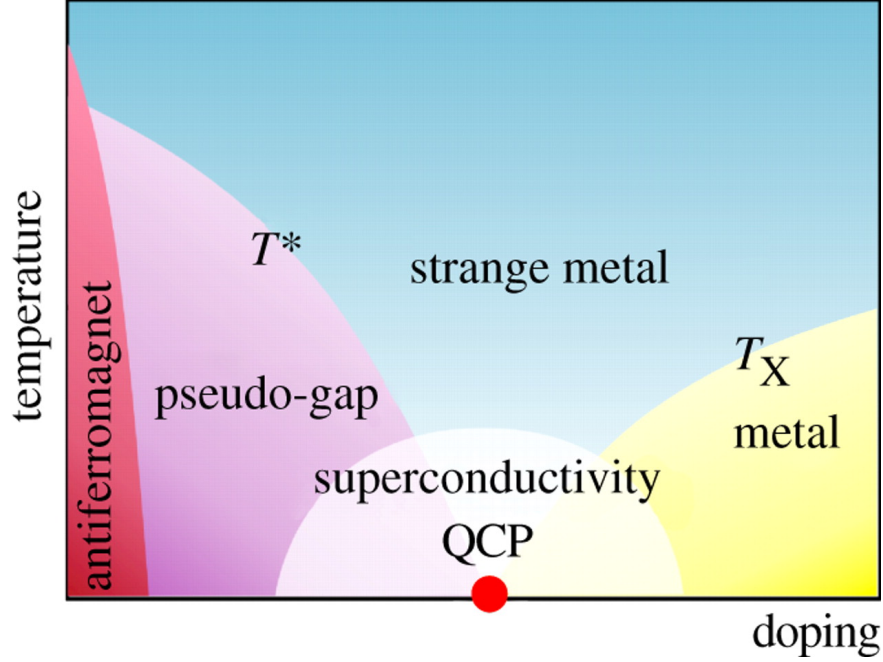


FIGURE 1.1: Qualitative phase diagram [1] of the hole doped cuprates. The many phases near the superconducting dome highlight the competing interactions in this system. These interactions may contribute to the elevated critical superconducting temperature.

to the mechanism driving the high critical temperature. One possible avenue of investigation is highlighted by the unique phase diagram of the cuprates.

The cuprate phase diagram shows many interesting features beyond the superconducting dome. An illustrative diagram Fig. 1.1, qualitatively describes the many phases which occur near the hole doped superconducting region of the cuprates. The Fermi liquid becomes a strange metal phase at a crossover temperature T_x . The crossover temperature decreases as the system approaches half-filling. Another crossover occurs closer to half filling to a pseudogap phase at a temperature T^* . In this instance the temperature dividing the phases increases as the system approaches half-filling. The competition between phases so near to the superconducting temperature gives credence to the possibility that the interactions could contribute to the high critical temperature. Experimental efforts such as the evidence of a broken symmetry near the pseudogap temperature [10] and magnetic

order developing around the pseudogap state [11] show that a quantum critical point is possible near center of the superconducting dome. It is worthwhile to mention that there is no direct evidence of a quantum critical point.

A quantum critical point may be briefly described as a transition driven entirely by quantum fluctuations. A key indicator is that the transition occurs at $0K$ and therefore thermal fluctuations are completely frozen out. Clearly, it is beyond the reach of even the most sophisticated experimental setups to test a true zero temperature transition. Nonetheless the intriguing possibility has driven significant research [12] because of the various unusual behaviors in the non-superconducting normal states. While the quantum critical point is driven by quantum fluctuations at zero temperature, the residual features of a quantum critical point may be apparent at finite temperature [13]. One of the possible outcomes is the presence marginal Fermi liquid [14]. The main motivation of this thesis is to search for the marginal Fermi liquid using large scale numerical simulations, in particular for the three dimensional Hubbard model.

1.2 Solving Strongly Correlated Systems

The eponymous Schrodinger equation,

$$\hat{H} = -\frac{\hbar^2}{2m}\nabla^2 + V, \quad (1.1)$$

describes the general information required to correctly model a quantum mechanical system. In a strongly correlated material the potential term, V , captures the interactions between subatomic particles. As the Coulombic force is present throughout the system the interaction term should include,

$$V_{coul} \propto \sum_{i,j} \frac{e^2}{|r_i - r_j|} \quad (1.2)$$

where the indices i, j account for each fermion in the system. Concerted efforts have yielded many possible methods for solving the mathematical problems of strongly correlated systems.

In general, it is rather difficult to solve the many body problem. Conventional methods include mean field approximation and summing certain classes of diagrams, such as the random phase approximation. Numerical methods are hampered by the exponential growth of the Hilbert space with respect to the number of electrons. Exact diagonalization based on solving the Hamiltonian matrix is limited to about 20 electrons. The infamous minus sign problem of quantum Monte Carlo limited the simulations to small system sizes or high temperatures [15]. The density matrix renormalization group is largely restricted to the one dimensional systems [16].

A breakthrough from the early nineties is the dynamical mean field theory, in which the interacting lattice problem is mapped to an impurity problem [17]. Rather accurate numerical methods were developed for such impurity problems during the seventies and eighties [18, 19]. This research chooses to follow the methods outlined by the dynamical mean field approximation, DMFA, and its cluster expansion the dynamical cluster approximation, DCA. This is chosen due to the accuracy and efficiency in the parameter regime of interest.

The thesis is organized as follows. In chapter 2, I discuss other properties of Fermi liquid, superconductivity, and the possible quantum critical point in the cuprates. In chapter 3, I explain the numerical method for solving the Hubbard model, these include the dynamical mean field theory and the dynamical cluster approximation. In chapter 4, I present the results from the dynamical cluster approximation for the three dimensional Hubbard model. We show unambiguously the existence of the marginal Fermi liquid, which is a smoking gun of the existence of a quantum

critical point. In chapter 5, there is a brief discussion of some efforts regarding the optimization of the parquet method utilizing the HPX runtime system. These efforts led to the improvement of network efficiency in the simulation and have a possible future in the automatic tuning of network parameters. I conclude in chapter 6 and discuss the possible future work to better understand the quantum critical point in three dimensional systems.

Chapter 2

Fermi Liquid Theory

For solid state and materials physics, the fundamental building blocks are electrons and phonons. This thesis focuses on systems of electrons on a lattice. As electrons are fermions, they obey the Pauli exclusion principal and must individually be described by a unique quantum state. Thus no two electrons can carry the same quantum numbers which in turn describe its quantum state. This fact, in combination with their indistinguishable nature, results in an antisymmetric wavefunction. These facts form the basic foundation for all theories involving systems of interacting electrons.

A real material composed of valence electrons whose number is on the order of 10^{23} appears to be a dauntingly complex system to solve. Even the most sophisticated computational techniques cannot solve such a system while tracking each element individually. The inclusion of interactions further increases the difficulty of solving such a system. A direct approach of analytically solving the generic interacting electron problem is intractable and a simplifying model is required.

These difficulties are most simply confronted by ignoring interactions altogether. Though this may seem to be a nonphysical assumption it yields surprisingly accurate solutions. Additionally, the Fermi liquid theory, FLT, comes directly from the foundation of the non-interacting system. Thus in an effort to motivate the FLT there is a brief discussion of the non-interacting system and some of its successful predictions.

2.1 Non-interacting Fermions: Fermi Gas

The non-interacting system serves as the basis for our understanding of metals. Though the fermions do not interact they are still confined to the lattice. The solu-

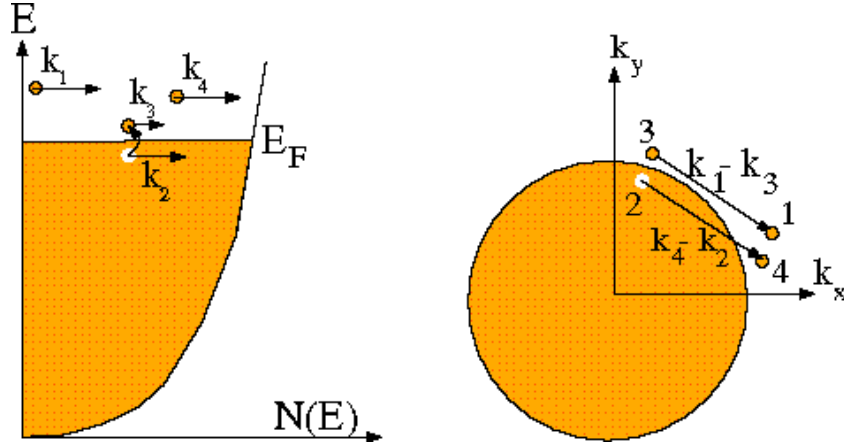


FIGURE 2.1: Qualitative view of electrons in a Fermi sea. The figure illustrates the scattering of two electrons in the presence of a filled Fermi sea. Conservation of momentum and energy require the outgoing states both be above the Fermi surface. Only a small shell of electrons occupy states sufficiently close to the surface to meet these requirements. This idea proves fundamental to understanding Landau's Fermi liquid theory.

tion to the Schrodinger equation for non-interacting fermions on a periodic lattice is a group of states known as Bloch waves [20]. Electrons fill these states starting at the lowest energy. The energy of the highest filled state is known as the Fermi energy. The Fermi temperature of macroscopic systems ($\sim 10^{23}$ electrons) is on the order of $10^4 K$ [21]. The resultant Fermi energy (ϵ_F) is $\sim 1eV$. In the presence of a filled Fermi sea there are no empty states below ϵ_F . At room temperature or below this allows only a small shell of electrons to participate in scattering as shown in Fig. 2.1.

The simplest model of a metal is the free electron model with its kinetic energy term given by the Hamiltonian (using theoretical units where $\hbar = 1$).

$$H = \frac{P^2}{2m} \quad (2.1)$$

The wavefunction is simply given by the plane-wave solution

$$\Psi_k(r) = \exp(ikr), \quad (2.2)$$

with the eigenenergy given by

$$\epsilon_k = \frac{k^2}{2m}. \quad (2.3)$$

For fermions the electron is spin 1/2, we assume working on a spin diagonalized basis. A general eigenstate is labeled by the momentum and the spin index.

Usually we consider the system in a finite volume, assuming that the system has d dimensions. The relation between volume and the linear dimension is given as $\Omega = L^d$. A finite system size comes with the quantization of energy as a consequence of satisfying the boundary condition. For example, the periodic boundary condition requires $\Psi(x+L) = \Psi(x)$. This requirement can be fulfilled by a discrete momentum, and thus the discrete energy as given by

$$k_x = \frac{2\pi n_x}{L}. \quad (2.4)$$

An important quantity to consider for systems of electrons is the excitation spectrum or spectral function as the energy level can be computed exactly in the non-interacting limit. The spectrum is a set of delta function peaks, with widths tending to zero.

$$A(\omega) = \frac{1}{N} \sum_i \delta(\epsilon_i - \omega). \quad (2.5)$$

N is the normalization factor equal to the number of particles in the system. It is important to realize that the spectral function is a crucial feature used to distinguish the non-interacting system from the Fermi liquid for which interaction are always present. As is shown below the delta function energies become smeared out in the case of the Fermi liquid.

We can further understand that from the relation between the spectral function and the Green function. The spectral function can be obtained via the retarded Green function as follows

$$A(k, \omega) = -\frac{1}{\pi} \text{Im}(G^R(k, \omega)). \quad (2.6)$$

In order to have a delta function as expected for free electron gas, the retarded Green function must be in the following form

$$G^R(k, \omega) = \frac{1}{\omega + i\eta - \epsilon_k}. \quad (2.7)$$

Consider the excitation in real time,

$$\exp(-i\epsilon_k t) \Psi^\dagger(k) |0\rangle, \quad (2.8)$$

in which $|0\rangle$ is the ground state formed by the filled electrons up to the Fermi surface and Ψ^\dagger adds a particle to the system. This oscillates in time. Careful thought reveals that a key feature of interaction is to dampen this oscillation.

Another important concept of electron systems is the existence of the Fermi surface. As the electron is a half odd integer spin particle, according to the spin-statistics theorem first discussed by Pauli, the wavefunction is anti-symmetric with respect to the swap of two electrons. At zero temperature the Fermi energy, which is the energy of highest energy state an electron occupies, is defined as

$$E_F = \frac{k_F^2}{2m}. \quad (2.9)$$

Electrons follow the Fermi-Dirac distribution given by

$$f(\epsilon) = \frac{1}{\exp(\beta(\epsilon - \mu)) + 1}, \quad (2.10)$$

where β is the inverse temperature. This equation also introduces the concept of chemical potential, μ , which controls the electron density of the system.

As the temperature approaches 0 thermal excitations become less and less common. Due to the spin statistics, Hund's rule, limiting the occupation of each energy level to a single particle each energy is occupied up to the eponymous Fermi energy. At 0K there is a sharp drop in probability of states being occupied at the Fermi energy. As show in Fig. 2.2 the occupation probability acts as a step function at the

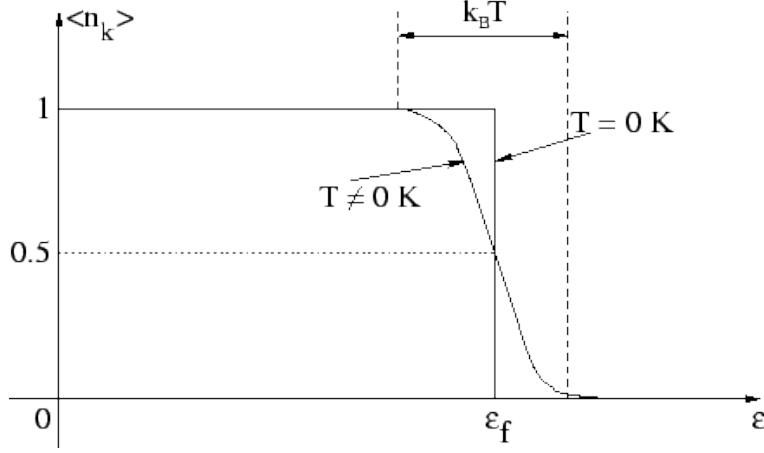


FIGURE 2.2: A qualitative view of Fermi statistics at and near $0K$. The occupation of all energy states up to the Fermi energy, ϵ_f by non-interaction electrons at 0 temperature. The probability drops to 0 above the Fermi energy while being exactly at 1 below it. Above $0k$ the electrons near ϵ_f are excited and the probability is lowered in equal measure with the excited states

Fermi energy. This feature forms what is known as the Fermi surface. The surface is the collection of energies below which the particles occupy all available energies and above Fermi energy the energy levels are unoccupied. The actual form of the Fermi surface depends upon the system being studied.

As we will mostly focus on the so-called tight-binding model in this thesis, here we introduce the concept of Wannier function and the local basis. Wannier function is an orthonormal basis. This basis can be represented as

$$\langle r|\phi_i\rangle = \phi_{R_i}(r), \quad (2.11)$$

the explicit functional form of this basis is not important for the discussion here. Physically, they can be considered as a highly localized orbital, for example, $\langle r|\phi_i\rangle$ is the orbital centered around R_i .

Assuming each local atom has a potential energy term E_i . As the Wannier function is presumably highly localized, the overlap among different orbitals at different locations is small and quickly decaying as a function of distance. This

argument is the fundamental justification of the tight binding approximation.

$$H = \sum_i E_i |i\rangle\langle i| + \sum_{i,j} (t_{i,j} |i\rangle\langle j|), \quad (2.12)$$

where $t_{i,j}$ is the overlap between orbital i and j . In the extreme limit, the overlap is restricted to nearest neighbors. Say, we have a lattice with the geometry of a one dimensional chain. The Hamiltonian can be written as

$$H = \sum_i E |i\rangle\langle i| + \sum_i t_i (|i\rangle\langle i+1| + |i+1\rangle\langle i|), \quad (2.13)$$

in a matrix representation. This Hamiltonian in the Wannier basis is an $N \times N$ matrix, with diagonal elements equal to E , and off-diagonal and super-diagonal elements equal to t . The boundary condition will decide the element in the bottom left and the top right corners. For periodic boundary condition they are both equal to t . For open boundary condition they are both equal to 0. A more generic boundary condition is possible, but we will not discuss it here. For the rest of this thesis, we will take the periodic boundary condition. With translational invariance we can diagonalize the Hamiltonian analytically and obtain the cosine band for the tight binding model

$$H = \sum_k (-2t \cos(k) + E) |k\rangle\langle k|, \quad (2.14)$$

with $k = 2\pi/n_i$.

As the energy eigenstate can be exactly calculated, the spectral function and the density of states can also be calculated, albeit not necessarily analytically. The key message is that the spectral function is still composed of a sum of delta functions like that of the electrons in free space.

As we will discuss the thermodynamics of the Fermi liquid in the following, they turn out to be very similar to the free fermion case. We briefly discuss the heat capacity of tight binding model.

At finite temperature the total energy of the system is given by

$$E(T) = \sum_k f_F(\epsilon_k - \mu) \epsilon_k, \quad (2.15)$$

the chemical potential is temperature dependent for the following argument it can be ignored. At finite but low temperature, only electrons near the Fermi level can be excited. The thermal energy is proportional to $k_B T$. Therefore the number of excited electrons should be given as

$$\Delta N(T) \sim k_B T N(E_F), \quad (2.16)$$

and thus the total energy due to electron excitations from thermal bath is given as

$$\Delta E(T) \sim (k_B T)^2 N(E_F). \quad (2.17)$$

Taking the derivative with respect to temperature, we obtain the heat capacity.

$$\Delta C(T) \sim k_B^2 N(E_F) T. \quad (2.18)$$

This is an important relation as even in the presence of interactions, the linear dependence on temperature remains unchanged for Fermi liquid.

2.2 Interacting Fermions: Fermi Liquid

The difficulty of satisfactorily explaining the dynamics of a system with many interacting particles encapsulates the field of many body physics. The non-interacting model shows significant promise in spite of its apparent nonphysical nature. Interactions increase the complexity of solving the Hamiltonian such that analytic solutions are largely unknown. In order to capture the physics of the interactions the problem requires significant simplification. A common approach would be to look for a small parameter and a solution about that small parameter. This is difficult in the case of the Coulombic interactions as the potential and the kinetic

energies are on the same order. Thus there is no apparent small factor for a perturbative approach. Any theory additionally should explain how the non-interacting system correctly captures many of the key features of metals.

Landau realized the key explanation of why the non-interacting system captures so many physical features of metals. The non-interacting electron gas fills states so completely at low temperatures that there are few states for electrons to excite to. At exactly zero temperature the only states available are the states above the Fermi energy.

In order for an interaction to occur the particles must scatter from some state to another. Free electrons occupy all available states up to the Fermi energy. The result is that an electron above the Fermi energy must scatter off an electron within the Fermi sea. In order for this scattering to be considered it must be long lived. These are the considerations Landau used to construct his Fermi Liquid Theory.

The scattering must therefore occur on or near the Fermi surface. This phase space restriction gives the limitation necessary for a continuation from the basis of the non-interacting electron model. This leads to the concept of quasiparticles. These are excited states of electrons in a Fermi liquid. They are inherently long lived near the Fermi surface. As their energy approaches the Fermi energy their lifetime becomes infinitely long lived. These quasiparticles have a defined momentum and energy. They act as particles but with a few modified features.

One of the notable modifications is the renormalized mass of the quasiparticle. The renormalized mass occurs as a result of the cloud of electrons around the quasiparticle. It therefore responds more slowly than a free electron would respond to forces. This reduction in the response can be treated as a renormalized mass of the particle. In a Fermi liquid the masses of the quasiparticles can deviate quite strongly from the bare electron mass.

Fermi liquid theory stands as the cornerstone of understanding the metallic phase of most systems. A low energy excitation serves as an example of the restrictions the occupied states place on scattering. A scattering process begins with an incoming electron with momentum and energy \mathbf{p}_1, ϵ_1 above the Fermi surface. It scatters off an electron in the Fermi sea with momentum and energy, \mathbf{p}_2, ϵ_2 . The outgoing electrons have momentum, $\mathbf{p}_3 = \mathbf{p}_1 - \mathbf{q}, \mathbf{p}_4 = \mathbf{p}_2 + \mathbf{q}$ and energy ϵ_3, ϵ_4 . From the conservation of momentum and energy,

$$\mathbf{p}_1 + \mathbf{p}_2 = \mathbf{p}_3 + \mathbf{p}_4, \epsilon_1 + \epsilon_2 = \epsilon_3 + \epsilon_4. \quad (2.19)$$

As we are interested in the low energy excitations only, the incoming energy ϵ_1 is close to the Fermi energy. It scatters a state below the Fermi surface to a state above the Fermi surface resulting in a change in energy $\delta\epsilon$. As there are no available states below the Fermi surface the final state of incoming electron must also be above the Fermi energy, $\epsilon_1 - \delta\epsilon > \epsilon_F$. The number of states available for such a scattering process roughly scales as $(\epsilon_1 - \epsilon_F)^2$.

Fermi liquid theory assumes that interactions do not destroy the free particle picture [22]. Adiabatically introducing interactions to the system evolves the system without leaving the ground state. With interactions, the particles' state remains unchanged but their properties such as mass are renormalized. The excitations should exist for a longer time than is required to turn on the interactions. That is if t is the time taken to introduce interactions to the system, then the lifetime of the excitation, τ , should be much greater than t . The excitations have the name quasiparticles due to their long lifetime near the Fermi surface. An estimation of the transition probability using Fermi's Golden rule gives the order of the quasiparticle lifetime [23],

$$1/\tau = \int d\mathbf{p}_1 \int d\mathbf{p}_2 \text{Im} \left(\frac{|U(\mathbf{q})|^2}{\epsilon_1 + \epsilon_2 - \epsilon_3 - \epsilon_4 - i\delta} \right), \quad (2.20)$$

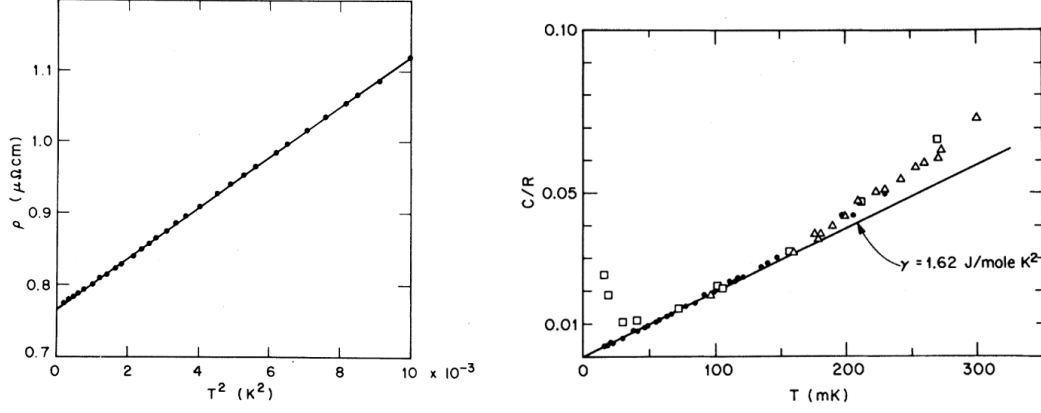


FIGURE 2.3: Specific heat at different field strengths and resistivity of $CeAl_3$. The resistivity shows a clear T^2 dependence in agreement with Landau's Fermi liquid theory. The specific heat similarly shows a linear trend in temperature even in the presence of a strong field. Images from [24].

where $U(\mathbf{q})$ is the interaction matrix element which should be only weakly dependent on \mathbf{q} and $i\delta$ is an infinitesimal imaginary part to avoid poles on the real axis. The shell of states available for scattering processes is proportional to the temperature. As the scattering involves two such shells the transition probability scales as ϵ_1^2 . The decay rate of the excitation is proportional to T^2 . Thus as the temperature decreases the quasiparticles lifetime increases. Near the Fermi surface these quasiparticles can be very long lived and well defined.

The argument above can be demonstrated more precisely by considering the second order perturbation for the self-energy. Three diagrams are generated at the one loop level. If the particle-particle diagram is not considered as it leads to pairing instability at low temperature. Among them the zero sound particle-hole diagram has the main contribution [25],

$$\sum_{\mathbf{k}} U(\mathbf{q})^2 \frac{f_{\mathbf{k}+\mathbf{q}} - f_{\mathbf{k}}}{\omega - (E_{\mathbf{k}+\mathbf{q}} - E_{\mathbf{k}}) + i\eta}. \quad (2.21)$$

This diagram is dominated when the scattering or momentum transfer, q is small. That is when $E_{\mathbf{k}}$ is close to the $E_{\mathbf{k}+\mathbf{q}}$. This is precisely the phase space restriction argument previously explained. Under this circumstance we can approximate the

energy difference as $\mathbf{q} \cdot \mathbf{v}_{\mathbf{k}}$. The diagram can be rewritten as

$$\sum_{\mathbf{k}} U(\mathbf{q})^2 \frac{\mathbf{q} \cdot \mathbf{v}_{\mathbf{k}}}{\omega - \mathbf{q} \cdot \mathbf{v}_{\mathbf{k}} + i\eta} \frac{df}{d\epsilon_{\mathbf{k}}}. \quad (2.22)$$

Assuming the interaction is independent of the momentum transfer, which is precisely the case for Hubbard interaction, the imaginary part of the particle-hole susceptibility from the zero-sound contribution can be readily obtained as

$$Im\chi(\mathbf{q}) = U^2 \pi N(\epsilon_f) \frac{\omega}{\mathbf{q} \cdot \mathbf{v}_{\mathbf{f}}}. \quad (2.23)$$

From the susceptibility, the self-energy can be obtained readily as

$$Im\Sigma(\mathbf{k}, \omega) = U^2 N(\epsilon_f) \frac{\omega^2}{\epsilon_f^2}, \quad (2.24)$$

for three dimensions, and there is an logarithmic correction for two dimensions.

This ω^2 dependence in the imaginary part of the self-energy can be seen as a defining property of the Fermi liquid. While we only show the argument at the one-loop level, it can also be demonstrated that the Fermi liquid is stable for summing the zero sound diagrams at higher orders [26, 27]. A more complete argument can be formed by consider the channel mixing among the three diagrams, which can be handled via the technique of functional renormalization group [28].

From these features of Landau's Fermi liquid theory stem many of its greatest successes. The specific heat is linear with respect to temperature as the theory predicts. Experimental verification of these features, Fig. 2.3, demonstrate the theory's strength.

Once we have the Fermi liquid theory established there is the matter of what good does it do for us. The Fermi liquid theory motivation primarily rested upon explaining He³ [27]. The theory does a fairly good job of explaining the metals on the first two rows of the periodic table. It explains the electronic contribution of the specific heat. It similarly predicts that resistivity should be dependent upon

T^2 . These results confirmed that this was in fact a good explanation of metals and gave a good qualitative explanation of many features of metals.

The phase space argument set forth previously represents a fairly strong explanation for why a metal should be a Fermi liquid. There is not any space available for alternatives to exist. In this manner it becomes somewhat surprising that there are in fact other types of metals.

The restrictions on phase space make Fermi Liquid theory robust. Even in the presence of strong interactions quasiparticles have so few states available that metals behave as a modified Fermi gas. One modification is the effective mass of the quasiparticle. Approximating the energy with a linear expansion in momentum gives [23],

$$\epsilon_1 - \epsilon_F = \frac{\mathbf{p}_1^2}{2m} - \epsilon_F \approx \frac{\mathbf{p}_F}{m^*}(\mathbf{p}_1 - \mathbf{p}_F). \quad (2.25)$$

m^* is the effective mass of the quasiparticle. The effective mass can in experiment be substantially different from a bare electrons mass. For instance in $CeAl_3$ as shown in Fig. 2.3 $m^* \sim 10^3 m$.

The Landau theory of Fermi liquid basically explains all metals except some special circumstances. The most notable one is in one dimension, for which the phase space argument clearly is not valid. There is an effective bosonic description for the one dimension case. Other known examples include multi-channel Kondo impurity models and possibly disorder Kondo impurity models.

Another plausible scenario for breaking the Fermi liquid is the effect from the quantum critical point, in which long distance fluctuations are large. In this instance the interactions would be so strong that the Fermi liquid would be destroyed. Instead there are metallic states that are strange metals which do not possess the properties of the Fermi liquid. The existence of strange metals has been an important topic in condensed matter physics since the early days of the high temperature

superconducting cuprates. It is widely believed that a key of understanding the high temperature superconductor is to understand the non-Fermi liquid state [29]. This topic has been studied extensively over the last three decades in two dimensions. However, there are few contributions in the study of possible non-Fermi liquid states in higher dimensions. Particularly, there is, far as we known, no unbiased numerical studies for the three dimension cases. A major part of this thesis is to fill this void. We will employ the state-of-the-art dynamical cluster approximation to study the doped three dimensional Hubbard model and investigate the possible non-Fermi liquid state.

In particular we will focus on the possibility of the marginal Fermi liquid. In order for the Fermi liquid's quasiparticle concept to survive, the lifetime or equivalent the width of the quasiparticle peak, must be smaller than ω . If not the coherent quasiparticle cannot be defined any more, as it cannot be normalized. As the width of the quasiparticle peak is given by the imaginary part of the self-energy, $Im\Sigma(\mathbf{k}_f, \omega)$, hypothetically, the self-energy can scale with respect to the energy as $Im\Sigma(\mathbf{k}_f, \omega) \propto \omega^\alpha$. The case of $\alpha = 1$ is the borderline for a well define coherent quasiparticle to exist [14].

We extend our discussion of the spectral function for the non-interacting Fermi gas to that of the Fermi liquid. For an interacting system, the effect of the single particle quantity can be summarized in terms of the self-energy. That is the contributions of the interactions are gathered in a self-energy term which is complex and depends on k, ω . In this way the interaction effects are simply written in the Green function equation. The relation between the self-energy and the Green function can be expressed as

$$G^R(\mathbf{k}, \omega) = \frac{1}{\omega + i\eta - \xi_{\mathbf{k}} - \Sigma^R(\mathbf{k}, \omega)}, \quad (2.26)$$

we incorporated the chemical potential into ξ_k defining $\xi_k = \epsilon_k - \mu$. The spectral function can be extracted from the imaginary part of the retarded Green function.

$$\begin{aligned} A(\mathbf{k}, \omega) &= \frac{-1}{\pi} \text{Im}[G^R(\mathbf{k}, \omega)] \\ &= \frac{-1}{\pi} \frac{\text{Im}[\Sigma^R(\mathbf{k}, \omega)]}{(\omega - \xi_{\mathbf{k}} - \text{Re}[\Sigma(\mathbf{k}, \omega)])^2 + \text{Im}[\Sigma(\mathbf{k}, \omega)]^2} \end{aligned} \quad (2.27)$$

The Fermi liquid can be understood from the functional form of the self-energy. As the heuristic arguments above, the imaginary part of the self-energy is proportional to the square of the energy scale. At zero temperature near the Fermi surface. It is given as

$$\text{Im}[\Sigma^R(\mathbf{k}, \xi_{\mathbf{k}})] \sim |\mathbf{k} - \mathbf{k}_f|^2. \quad (2.28)$$

At low temperature and low energy, it is given as

$$\text{Im}[\Sigma^R(\mathbf{k}, \omega)] \sim -(\omega^2 + \pi^2 T^2) \quad (2.29)$$

This can be seen as the definition of the Fermi liquid.

We first consider the real part of the self-energy.

$$\begin{aligned} \omega - \xi_{\mathbf{k}^0} - \text{Re}[\Sigma^R(\mathbf{k}, \omega)] &= \\ &\approx \omega - \xi_{\mathbf{k}}^0 - \text{Re}[\Sigma^R(\mathbf{k}, \omega)] - (\omega - \xi_{\mathbf{k}}) \partial_{\omega} \text{Re}[\Sigma(\mathbf{k}, \omega)]|_{\omega=\xi_{\mathbf{k}}} \\ &\equiv \frac{\omega - \xi_{\mathbf{k}}}{z_{\mathbf{k}}}, \end{aligned} \quad (2.30)$$

with this definition, we can relate the damping to the imaginary part of the self-energy

$$\frac{1}{\tau_{\mathbf{k}}} = -2z_{\mathbf{k}} \text{Im}[\Sigma^R(\mathbf{k}, \xi_{\mathbf{k}})]. \quad (2.31)$$

The spectral function can then be written as

$$A(\mathbf{k}, \omega) \approx \frac{z_{\mathbf{k}}}{2\pi} \frac{1/2\tau_{\mathbf{k}}}{(\omega - \xi_{\mathbf{k}})^2 + (1/2\tau_{\mathbf{k}})^2}. \quad (2.32)$$

This is the spectral function of the Fermi liquid. The integration of the spectral function over energy should be conserved, $\int_{-\infty}^{\infty} d\omega A(\mathbf{k}, \omega) = 1$. Therefore there is another part of the spectral function which contributes to the missed $1 - z_{\mathbf{k}}$ of the spectral weight. The physical meaning of the Fermi liquid spectral function is clear, as this is a Lorentzian function with width of $\tau_{\mathbf{k}}$ and peak value $z_{\mathbf{k}}$ at energy $\xi_{\mathbf{k}}$.

We can also consider the excitation in the Fermi liquid in real time, as we saw for the non-interacting case it is oscillatory and has no damping. In the Fermi liquid, it is

$$\exp(-i\xi_{\mathbf{k}}t - t/(2\tau_{\mathbf{k}}))\Psi^{\dagger}(\mathbf{k})|0\rangle. \quad (2.33)$$

This shows explicitly the physical meaning of $\tau_{\mathbf{k}}$ is a damping factor.

The $z_{\mathbf{k}}$ has an important physical implication. This is the main quantity which distinguishes the Fermi liquid from non-Fermi liquid. We can calculate the momentum distribution near the Fermi level, this will reveal the physical meaning of $z_{\mathbf{k}}$. The momentum distribution function can be written in terms of the Matsubara Green function

$$\langle \Psi_{\mathbf{k}}^{\dagger} \Psi_{\mathbf{k}} \rangle = G(\mathbf{k}, \tau = 0^-) = \frac{1}{\beta} \sum_{\omega_n} \exp(i\omega_n \eta) G(\mathbf{k}, i\omega_n). \quad (2.34)$$

At zero temperature, it is related to the spectral function simply as the sum up to the Fermi energy, which we take as 0, that is

$$n(k) = \int_{-\infty}^0 d\omega A(\mathbf{k}, \omega). \quad (2.35)$$

As we know the form of the spectral function for low energy near the Fermi surface, we can plug it into this equation to calculate the momentum distribution function. Recall that the damping, or the scattering rate, decays as a square of excitation energy. We can assume that at the Fermi level it can be neglected. That is the

spectral function becomes a delta function with height given, that is $A(\mathbf{k}_f, 0) \sim z_{\mathbf{k}} \delta(\omega - \xi_{\mathbf{k}})$

If we consider the change of the momentum distribution function across the Fermi level, that is

$$\langle \Psi_{\mathbf{k}_f^+}^\dagger \Psi_{\mathbf{k}_f^+} \rangle - \langle \Psi_{\mathbf{k}_f^-}^\dagger \Psi_{\mathbf{k}_f^-} \rangle. \quad (2.36)$$

This can be related to the $z_{\mathbf{k}}$. Therefore there is a jump in the momentum occupation number across the Fermi level.

$$\langle \Psi_{\mathbf{k}_f^-}^\dagger \Psi_{\mathbf{k}_f^-} \rangle - \langle \Psi_{\mathbf{k}_f^+}^\dagger \Psi_{\mathbf{k}_f^+} \rangle = z_{\mathbf{k}}. \quad (2.37)$$

In contrast to the free electron gas, the jump is reduced from 1 to $z_{\mathbf{k}} < 1$, however the discontinuity in the momentum occupation number remains intact. This is a defining feature of Fermi liquid. One of the main goals of this thesis is to use state-of-the-art numerical method to determine this $z_{\mathbf{k}}$ factor.

2.3 Conventional Superconductivity

Superconductivity is an interesting phase of many metals which emerges at low temperatures. Conventional superconductors are well explained by the BCS theory [30, 31, 32, 33]. The free Fermi gas, which is a Fermi liquid, serves as the starting point of the BCS theory. A key idea in the BCS theory is the formation of electrons pairs in the presence of an attractive interaction. These pairs are commonly known as Cooper pairs, named after Leon Cooper the scientist to explain the phenomena. The pairing susceptibility diverges below a critical temperature. This divergence signals a phase transition from a Fermi liquid to a phase with long range ordering of electron pairs which are responsible for the superconductive phase. Starting from the bare pairing susceptibility and adding in interaction terms the approximated susceptibility by summing the so-called ladder diagrams can be constructed as shown in Fig. 2.4.

$$\chi_{pair} = \text{---} \rightarrow \text{---} + \text{---} \text{---} \text{---} + \text{---} \text{---} \text{---} + \dots$$

FIGURE 2.4: Ladder diagrams of pairing susceptibility. This is a diagrammatic representation of pairing susceptibility of a Fermi liquid. The summation of ladder diagrams results in a geometric series whose sum is dependent only on g, χ_0

In this diagram the lines are the Green function of the system. The oscillating line represents the attractive interaction (g) between the electrons. These ladder diagrams form an infinite series. This series is recognized as a geometric series. Thus the result only depends upon the interaction strength and the bare susceptibility,

$$\chi_{SC}^{RPA} = \frac{g}{1 - g\chi_0}. \quad (2.38)$$

This equation diverges when $1 - g\chi_0 = 0$. The bare pairing susceptibility can be used to define the critical temperature for the superconducting state. This is

$$T_c \propto \omega_c e^{\frac{1}{gN(0)}} \quad (2.39)$$

where ω_c is the cutoff frequency often taken to be the Debye frequency and $N(0)$ is the density of states.

The BCS theory of superconductivity describes conventional superconductors well. A key feature of the BCS theory was the ability to explain the gap seen in conventional superconductors [34]. Additionally, this theory explained other experimentally observed features, such as the isotope effect [35] and variation of the gap as the temperature [36] of the superconductor approached the critical temperature.

The explanation of the robustness of Landau's Fermi liquid theory appears to give an elegant explanation for how metals should react especially at low temperatures. It is then a surprise when materials exhibit behavior which deviate from this theory. A notable example are the cuprate high temperature superconductors.

2.4 Cuprate Superconductor

An example of materials contradicting the conventions of BCS theory are the cuprates [37]. These are compounds whose superconducting temperature is notably higher than that of the conventional superconductors. The name, cuprate, derives from planes of Cu_2O separated by an insulating layer. In these materials the superconducting temperature is highly doping dependent. As such, there is a under-doped and an over-doped area of the phase diagram where the critical temperature diminishes. The theoretical explanation of high temperature superconductivity remains highly controversial. Nonetheless, considerable experimental efforts have found interesting features in the cuprate phase diagram even outside the superconducting regime.

The normal state properties of the cuprates do not always behave as a Fermi liquid [38]. At optimal doping the resistivity is linearly dependent on temperature as seen in Fig. 2.5. The $Br_2Si_2CaCu_2O_{8+x}$ compound's resistivity maintains a power law dependence on temperature even when not at an optimal doping. This demonstrates the deviation from Fermi liquid character for a variety of dopings. As cuprates are notably 2D in character, these measurements were taken in the direction of the $Cu - O$ plane.

Another result is the study of the Fermi surface. This is studied by angle resolved photoemission spectroscopy, ARPES, which is particularly suited to the study of Cuprates. This is due to the fact that ARPES studies two dimensional materials particularly well. The optimally doped cuprate Fermi surface contains filled states at the center of the two dimensional Brillouin zone with empty states near its corners. The density of filled states versus empty states generally matches the particles contributed by the parent compound and the holes from the doped material. This fits well with the Fermi liquid picture.

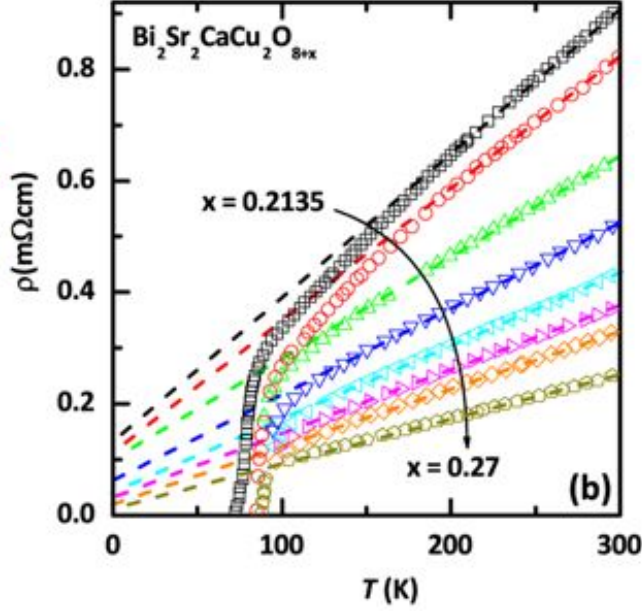


FIGURE 2.5: Resistivity of $\text{Bi}_2\text{Sr}_2\text{CaCu}_2\text{O}_{8+x}$ at various concentrations. The colored lines represent the values of x in the formula. All measurements demonstrate the features of the strange metal phase through the linear resistivity. The resistivity indicates the cuprate is not a Fermi liquid before it enters its superconducting state. This data was gathered from [38].

The pseudogap is a separate phenomena from the superconducting gap as it exists outside the superconducting state. It presumably has no long range ordering, but the spectral function has similar structure as that of the superconducting phase. The formation of an excitation gap has been found in the specific heat, spin susceptibility, spin relaxation rate from nuclear magnetic resonance and also directly measuring the spectrum using ARPES. It is seen as a state that is separate and possibly competing with the superconducting state. Evidence for its existence include the deviation of the condensation energy from the BCS value when hole doped away from its critical value. At and above critical doping the pairing condensation energy is consistent with the prediction from the BCS theory for d-wave pairing. In the underdoped regime the condensation energy decreases much more quickly than the BCS value. This decrease may suggest that the expected d-wave gap is modified and possibly related to the formation of pseudogap.

The NMR studies of the cuprate superconductors additionally shed light on the character of the superconducting state. It shows that the pair wavefunction has a singlet form. There is some discussion as to whether these experiments show nodes in the gap. Measuring the inverse spin lattice relaxation time, $\frac{1}{T_1}$, shows $\frac{1}{T_1} \propto T^3$ [39]. The cubic dependence serves as another evidence of d-wave symmetry. Particular care should be taken when considering this as the low temperature NMR studies are sometimes unreliable. These measurements require very pure samples which are not always reliably obtained.

Another interesting feature of the high T_c superconductors is the electronic specific heat, C_{el} . For the Fermi liquid the electronic part of the specific heat is given by,

$$C_{el} = \gamma T, \quad (2.40)$$

where $\gamma = \frac{2\pi^2}{3} k_B^2 N(0)$ and $N(0)$ is the density of state at the Fermi level. At critical doping the cuprate superconductors also have this form up to room temperature [40]. The quasiparticles enhance the mass by a factor of 4 compared to the free electron model. In the superconducting regime cuprate's specific heat discontinuously jumps. In a BCS superconductor the specific heat takes the form of a decaying exponential. In contrast the cuprate superconductors specific heat is quadratically dependent on temperature. The difference highlights that the gap is not longer a symmetric gap. This is an important piece of evidence for the existence of a d-wave gap.

In Cuprate superconductors, the gap that opens contains nodes unlike the symmetric gap of BCS superconductors. This experimental result has been confirmed after much effort using phase-sensitive Josephson experiment. Superficially, two different setups of Josephson experiment are used extensively for the cuprates, these include the superconductor-normal metal-superconductor junction and the

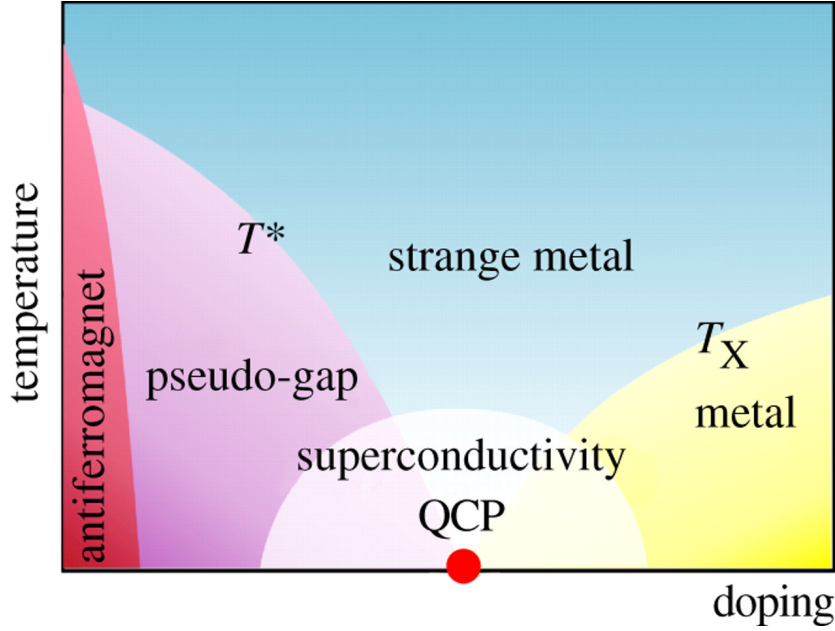


FIGURE 2.6: Qualitative phase diagram of the cuprates [1]. The pseudogap phase on the left of the superconducting dome with the Fermi liquid phase on the right. The strange metal phase exists in the middle above the superconducting dome. The combination of these phases implies the possibility of a quantum critical point in the center of the superconducting dome.

SQUID junction. All the experiments concluded that the pairing gap has a $d_{x^2-y^2}$ geometry.

In spite of a extreme amount of work in the field, there remains no consensus as to the proper theory for describing high temperature superconductivity. A notable difficulty is correctly accounting for cuprate superconductors many phases near the superconducting dome. Fig. 2.6 illustrates the phases near the superconducting dome. The combination of these phases serve to guide the eye towards a proposed quantum critical point in the center of the superconducting dome.

The interesting states of the cuprate superconductors are now briefly qualitatively discussed, for a more in depth discussion see the previous pages. The pseudo-gap phase is a phase where the states near the Fermi surface decrease significantly with respect to the number of states nearby. The energy is not completely devoid of states so the material does not form an actual gap. Above the peak of the super-

conducting dome a cuprate superconductor enters a “strange metal” phase. This phase is considered a strange metal phase as it does not follow the features of a Fermi liquid. For instance, the aforementioned linear temperature dependence of resistivity. One proposed explanation of this phase is a marginal Fermi liquid. A possible mechanism for the existence of the marginal Fermi liquid is based on the proximity to a quantum critical point.

Such a quantum critical point has been reported in the numerical simulations of the Hubbard model at two dimensions. The Hubbard model is a Hamiltonian for a system with a tight binding kinetic energy terms, usually with nearest and next-nearest hopping terms for modeling the copper oxide plane in the cuprates, and an on site interaction term [41],

$$H = -t \sum_{\langle ij \rangle} c_i c_j^\dagger - t' \sum_{\langle\langle ij \rangle\rangle} c_i c_j^\dagger + U \sum_i n_{i\uparrow} n_{i\downarrow}. \quad (2.41)$$

Though simple, this equation has no known general solution beyond 1D. Investigating its properties in three dimensions is one of the tasks of this research.

2.5 Quantum Critical Point

Traditionally the phase transition of statistical models is driven by the thermal fluctuations. The phase transition is defined as the discontinuity in the free energy or the derivatives of the free energy. Phase transitions fall into two different categories, the first order phase transition with discontinuous free energy; and the second order phase transition with discontinuous first derivative of the free energy.

A distinctive feature of the second order transition is the divergence of the correlation length. Precisely because of this property, the short distance physics becomes irrelevant as the main factor which drives the transition is due to the divergence in the long distance correlations. Therefore, many seemingly different second order phase transitions can be classified into few different universality classes. The main

idea is that the short distance couplings could be rather complicated, but near the second order phase transition the physics is determined by the divergence length scale which is the correlation corresponding to some ordering.

A beautiful theory which encapsulated the thermal phase transition is the Landau theory [42]. Within this theory, a phase transition is accompanied with a broken symmetry—the symmetry can usually be defined by a local order parameter. A simple example of an order parameter is the magnetization of a ferromagnet. The free energy can be written as a power series expansion of the order parameter. The transition happens when the free energy is minimized by a finite order parameter. The Landau theory basically encapsulated most of the phase transitions until very recently.

Before embarking the discussion of quantum phase transition, a digression to the path integral prospective of quantum mechanics and its relation with classical statistical mechanics will prove to be helpful. The thermodynamics of a classical system is encoded in the partition function which is given by the Boltzmann distribution of summing over all the admissible phase space. Formally it can be written as $\int dpdq \exp[-\beta H(\{p, q\})]$. For classical systems the kinetic energy and the potential energy can be factorized, that is $H(p, q) = T(p) + U(q)$, in which the kinetic energy can usually be calculated exactly. The calculation is then boiled down to calculating the partition function for the potential energy, $Z \sim \int dq \exp(-\beta U(q))$.

On the other hand, the partition function of a quantum system is given as the trace of the exponential of the Hamiltonian operator, $Z = \text{Tr} \exp(-\beta H)$. The major difficulty is that the contribution of kinetic energy and potential energy is, in general, not factorizable. By using the Trotter-Suzuki approximation, the

partition can be approximated by cutting the exponential into products,

$$Z = \lim_{N \rightarrow \infty} [\exp(-\beta T/N) \exp(-\beta U/N)]^N. \quad (2.42)$$

In the continuum limit, $Z = \int D[\phi(\tau)] \exp(S[\phi(\tau)])$. The action is given by the integrating the Lagrangian density over the space and time

$$S = \int d^d x \int_0^\beta d\tau \mathcal{L}(\phi, \nabla \phi, \partial_\tau \phi). \quad (2.43)$$

In the imaginary time formulation, the quantum action is effectively in the dimension of d spatial dimensions and 1 temporal dimension. In general, the temporal dimension does not scale as the spatial dimension and the dimension of the temporal dimension is usually denoted as z .

A quantum statistical system at d spatial dimensions can be effectively treated as a $d + z$ dimensions classical system in the imaginary time formulation [43]. There are cases in which additional terms not present in the classical systems need to be considered more carefully. A typical example is the path integral formulation of spin operators. Topological objects such as berry phase, which does not have a direct analogy in the classical theory, may be present. Besides such subtleties, in general as long as only thermodynamics is concerned, the major difference between classical and quantum systems is in the coupling between space and time.

Near the quantum critical point, there is a fan shaped area at finite temperature in which quantum critical scaling is expected. The shape of the fan is determined by the dynamical exponent [13]. Calculating those exponent in numerical simulations are rather difficult, given the limited systems sizes and the limited range of temperature for the simulations. A major work in this thesis is to determine the so-called quantum critical fan at low but finite temperatures, particularly for the Hubbard model at three dimensions.

Our intent is not to discuss the quantum phase transition in detail in this thesis. The purpose of this section is to highlight that a possible and indeed likely route to break away from the Fermi liquid is to have a long range interaction. Intuitively, the large quantum fluctuations near the quantum critical point provide the environment for an effective long range interaction to occur and thus a possible route of obtaining non-Fermi liquid.

Chapter 3

Numerical Solutions to the Hubbard Model

3.1 Hubbard Model

Microscopic many body systems contain moles of electrons and ion nuclei. Solving such a complex system exactly lies beyond the reach of both analytic and computational techniques. An approximation which successfully solves for the observables of many materials is known as density functional theory. While successful in modeling many systems, density functional theory fails when modelling systems where electron-electron interactions become significant. Such systems, known as strongly correlated systems, require additional effort to understand. Density functional theory fails in this case due to the effects of the interactions. In order to treat systems with strong correlations the Hamiltonian describing the system should directly include interactions. One of the simplest Hamiltonians fulfilling these demands is the Hubbard model.

The Hubbard Hamiltonian,

$$H = t \sum_{\langle i,j \rangle, \sigma} c_{i\sigma}^\dagger c_{j\sigma} + U \sum_i n_{i\uparrow} n_{i\downarrow} - \mu \sum_{i,\sigma} n_{i,\sigma}, \quad (3.1)$$

models a lattice with an onsite repulsion for doubly occupied sites. The first term treats the motion of electrons as hopping from one site to its nearest neighbor sites. This hopping term occurs via the destruction of an electron on one site and the creation of an electron on a neighboring site. The $c_{i\sigma}^\dagger, c_{i\sigma}$ are respectively the site i creation/annihilation operators. The hopping integral t can be thought of as representing the overlap of wave functions between neighboring sites. Since wave functions become exponentially small over large distances, it is reasonable to restrict hopping to only nearest neighbors. The Hubbard model rests on the simplification that the Coulomb interaction is strongly screened. It only includes

the onsite repulsion of doubly occupied sites as all other interactions are assumed to be screened. The Pauli principle restricts each lattice site to having at most two electrons with opposite spins. The second term of the Hubbard Hamiltonian accounts for the energy cost U of a doubly occupied site. The density operator $n_{i\sigma} = c_{i\sigma}^\dagger c_{i\sigma}$ counts the number of spin up/down particles at the i -th site. The chemical potential μ controls the filling of the system. The Hubbard model's simple form belies the difficulty of finding its general analytic solution. There is no known exact solution for a generic combinations of the parameters t , U , and μ in two or higher dimensions.

3.2 Green Function

As we are mostly interested in the single particle Green function in the dynamical mean field approximation and dynamical cluster approximation, we here recap the definition and key properties of it. One of the most important tools in many body physics is the Green function. It is versatile due to its strong theoretic foundation while giving access to some observable properties of the system.

In the following we introduce the Green function operator so that the object will be familiar in the theories presented. The imaginary time Green function is defined through the correlators of the creation and annihilation operators,

$$G_{ij}(\tau) = \langle T c_i(\tau) c_j^\dagger(0) \rangle. \quad (3.2)$$

Here i and j are locations on the lattice and τ is the imaginary time and T is the time ordering operator. The time ordering operator ensures the operator with the later time occurs on the left in the equation. The step function enables the mathematical representation of T ,

$$G_{ij}(\tau) = \Theta(\tau) \langle c_i(\tau) c_j^\dagger(0) \rangle + \Theta(-\tau) \langle c_j^\dagger(0) c_i(\tau) \rangle. \quad (3.3)$$

The average $\langle \dots \rangle$ is solved via the trace,

$$\langle \dots \rangle = \frac{Tr(e^{-\beta H} \dots)}{Tr(e^{-\beta H})}. \quad (3.4)$$

In practice the Green functions are most often calculated using imaginary time.

This formalism results in operators defined as,

$$\hat{A}(\tau) = e^{H\tau} A e^{-H\tau}. \quad (3.5)$$

This relates to the typical definition if one assumes that time is an imaginary quantity, hence the imaginary time nomenclature. In imaginary time the fermionic Green function is antiperiodic with a range of the inverse temperature $\beta = \frac{1}{T}$. Thus it is a periodic quantity over two times this range. These periodic qualities enable the Fourier transform into frequency space which gives

$$G(i\omega_n) = \int_0^\beta d\tau G(\tau) e^{i\omega_n \tau}. \quad (3.6)$$

Here the Matsubara frequency is defined as $\omega_n = 2\pi T(n + \frac{1}{2})$. Throughout this document the prefactor i and the subscript n will be assumed.

The Green function serves as the foundation of the theories presented in this thesis. They serve as propagators for the particles in the system. That is they give the probability amplitude of a particle traveling through space and time or its reciprocal space. Many of the theories build upon Feynman diagrams which are composed of Green functions. Diagrammatic perturbation theory builds from the quantity of the Green function. While this thesis does not explore the profundity of the findings of this theory it does lean on diagrammatics in its derivation. As such we introduce the basic elements



$$(3.7)$$

The propagator is defined by the straight line and an arrow while interactions are defined by an undulating line. The combination of these diagrams can then be used to formulate the perturbative expansion of Feynman diagrams.

An example of an extremely simple case where the Hubbard model is soluble is the non-interacting case. Letting $U = 0$ the Hubbard model simplifies to a Hamiltonian for non-interacting fermions on a lattice. In this case the dispersion comes in the form of a cos such that,

$$\epsilon_{\mathbf{k}} = -2t \sum_n^D \cos(k_n a). \quad (3.8)$$

On the other extreme the $t = 0$ the system enters the atomic limit which can again be solved. The intermediate case where both the hopping and the interaction play a strong role is far more difficult and interesting. From the perspective of the Green function introducing interactions modifies the quantity. The modification is captured by the self-energy, Σ . This leads to the definition of the full Green function through the Dyson equation

$$G = G^0 + G^0 \Sigma G \quad (3.9)$$

where G^0 is the free particle Green function. The Hubbard model is not solvable in the general case analytically. Generally the interaction term cannot be ignored, treated as a small parameter, nor factorized. In order to tackle this problem a variety of approaches were employed by various scientists. Hubbard, for example, employed a Green function decoupling method [44] and Brinkman and Rice [45] used the Gutzwiller variational method. These solutions were restricted to $T = 0$ and were unable to capture both the Mott metal-insulator transition, MIT, and the quasiparticle behavior simultaneously. In order to move beyond these limitations a new technique was required.

A well known numerical technique for simplifying such systems relies upon taking some parameter in the theory to be very large. Thus, if a factor that is the inverse of this parameter can be identified in the calculation, that value can then take the form of a small parameter. As an example is the Weiss theory for the Ising model where the interaction is of infinite range and the dimension of the system approaches infinity. In the Hubbard model the limit of infinite dimensions is once again very useful. This limit gives rise to the dynamical mean field approximation, DMFA.

The DMFA has been successful in identifying solutions to the Hubbard model. One of the main successes is the identification of the Mott metal to insulator transition. This is achieved practically through the solution partial differential equations through numerical techniques. Application of numerics is a necessity outside of few special cases for the Hubbard model.

Moving beyond a mean field solution to the Hubbard model would require the addition of a spatial dependence in the solutions or identically the addition of momentum dependence. The dynamical cluster approximation achieves this through coarse graining across multiple impurity sites. These methods are complex and important. As such these methods will be discussed in greater detail in the following sections of this chapter.

3.3 Dynamical Mean Field Approximation

The formulation of the DMFA recognizes the relationship of solving the Hubbard model to that of a single impurity problem. The diagrammatic expansion of the Hubbard model and the single impurity model are compared they are found to be identical. Solving the Hubbard Hamiltonian then is a self-consistent technique. A solution is obtained when the self-energy of the infinite dimensional Hubbard model and the impurity model are identical.

The subsequent equations and derivations will be presented in theoretical units where \hbar , a , and k_b are set to unity. In these units the density of states is the sum of delta functions about the energies found in the dispersion of the tight binding model.

$$N_d(\omega) = \sum_{\mathbf{k}} \delta(\omega - \epsilon_{\mathbf{k}}) \quad (3.10)$$

This density relates to the probability that a randomly selected ω is at the energy $\epsilon_{\mathbf{k}}$. This relationship allows for the application of the central limit theorem.

The central limit theorem states that the sum of a distribution of random variables will tend towards a normal distribution. This property holds regardless if the underlying distribution from which the variables are selected is a normal distribution [46]. Therefore with a randomly chosen set of ϵ_k the density of states emerges as a Gaussian having the form,

$$N_d \xrightarrow{d \rightarrow \infty} \frac{1}{2t\sqrt{\pi d}} \exp\left(-\left[\frac{\omega}{2t\sqrt{d}}\right]^2\right) \quad (3.11)$$

In order for the DOS to be normalizable there must be a relationship between the hopping and the dimensions. Specifically t must scale proportionally to the inverse of the square root of the dimension of the system. In the limiting case of free electrons the kinetic energy of the real space representation is

$$E_{kin} = -t \sum_{\langle ij \rangle} c_i^\dagger c_j. \quad (3.12)$$

Recognizing the relationship between this and the definition of the bare Green function 3.2 the kinetic energy is given by

$$E_{kin} = \lim_{\tau \rightarrow 0^-} -t \sum_{\langle ij \rangle} G_{ij}^0(\tau) \quad (3.13)$$

In order for the kinetic energy to be finite the factor of dimension must be removed from the equation. Thus each G^0 should contribute a factor of $\frac{1}{\sqrt{d}}$ as the number

of nearest neighbors scales as d . In this way the kinetic energy is now free of any dependence on dimension.

It is worth noting that though the hopping tends towards 0 in the limit of infinite dimensions the electrons in the Hamiltonian are not localized. Any such hopping incurs the cost

$$G_{ij}^0 \propto \frac{1}{d^{\|i-j\|}} \quad (3.14)$$

where $\|i-j\|$ is defined to be the number of hops through nearest neighbors to get from site i to site j . This fact proves essential to the DMFA. This scaling of the bare Green function results in the self-energy only including local terms as all other terms become infinitesimally small as the dimension becomes infinite. This is a foundational principle of the DMFA [47, 48, 49].

The above argument provides a basis of development of a mean field theory, that is a theory without explicit spatial dependence. It can be shown very transparently in the path integral formulation. Consider the action of the Hubbard model in a lattice,

$$S = \sum_{r,r'} \int_0^\beta \int_0^\beta d\tau d\tau' \sum_{\sigma} \psi_{\sigma}^*(r, \tau) G_0^{-1}(r, \tau, r', \tau') \psi_{\sigma}(r', \tau') \quad (3.15)$$

$$- U \sum_r \int_0^\beta \psi_{\uparrow}^*(r, \tau) \psi_{\uparrow}(r, \tau) \psi_{\downarrow}^*(r, \tau) \psi_{\downarrow}(r, \tau).$$

The first part of the action contains the kinetic energy as characterized by the bare Green function, it is simply given by the bare dispersion of the model being considered. The second term includes the interaction, which we assume to be a local interaction only. Any interaction beyond the local Hubbard term has to involve further approximation in the context of dynamical mean field theory.

The exact Green function of the above action can be completely characterized by the self-energy. For the simplicity of the discussion, we write the self-energy in

the frequency-momentum space, the relation between the bare Green function and the exact Green function is given by the Schwinger-Dyson equation

$$G(\mathbf{k}, \omega) = \frac{1}{G_0^{-1}(\mathbf{k}, \omega) - \Sigma(\mathbf{k}, \omega)} \quad (3.16)$$

The idea of the dynamical mean field theory is to relate the model without spatial dependence to the full model with spatial dependence. Stripping off the spatial dependence of the above action, we obtain

$$S = \int_0^\beta \int_0^\beta d\tau d\tau' \sum_\sigma \psi_\sigma^*(\tau) G_0^{-1}(\tau, \tau') \psi_\sigma(\tau') - U \int_0^\beta \psi_\uparrow^*(\tau) \psi_\uparrow(\tau) \psi_\downarrow^*(\tau) \psi_\downarrow(\tau). \quad (3.17)$$

This is exactly the action of the single impurity Anderson model with the hybridization given by the G_0 . The next assumption of the dynamical mean field theory is that the ‘best’ approximation of the full Hubbard model given by the single impurity Anderson model is obtained by matching the self-energy of these two models. This can be justified via the concept of "cavity method" by integrating out all degrees of freedom except one site, we denote it as site 0-th.

$$\frac{1}{Z_{eff}} \exp(-S_{eff}[\Psi_{0,\sigma}^* \Psi_{0,\sigma}]) = \frac{1}{Z} \int \prod_{i \neq 0, \sigma} \exp(-S[\{\Psi_{i,\sigma}^*, \Psi_{i,\sigma}\}]). \quad (3.18)$$

The effective action, S_{eff} , is given by the single impurity Anderson model.

Formally the connection between the lattice Hubbard model and the single impurity Anderson model is given as

$$\Sigma_{Hubbard}(\mathbf{k}, \omega) = \Sigma_{Anderson}(\mathbf{k}, \omega). \quad (3.19)$$

However, the self energy of the original Hubbard model has spatial dependence, but that of the single impurity Anderson model doesn't. For reconstructing the

exact Green function from the self-energy one has to rely on a process of coarse-graining, that is assuming the self-energy of the Hubbard model is the same in the entire first Brillouin zone.

$$G_{Hubbard}(\mathbf{k}, \omega) = \frac{1}{G_{Hubbard,0}^{-1}(\mathbf{k}, \omega) - \Sigma(\mathbf{k}, \omega)} \quad (3.20)$$

$$\approx \frac{1}{G_{Hubbard,0}^{-1}(\mathbf{k}, \omega) - \Sigma_{Hubbard}(\omega)}.$$

As discussed above, physically one can see that as the Hubbard model exists in infinite dimensions the missing link between the Hubbard model and the Anderson model is to determine the effective bare Green function of the Anderson model. This is given as

$$G_{0,Anderson}(\omega) = \sum_{\mathbf{k}} \frac{1}{(2\pi)^D} G_{Hubbard}(\mathbf{k}, \omega) \quad (3.21)$$

$$= \sum_{\mathbf{k}} \frac{1}{(2\pi)^D} \frac{1}{G_{Hubbard,0}^{-1}(\mathbf{k}, \omega) - \Sigma_{Hubbard}(\omega)}.$$

The bare density of state as discussed above can be exactly calculated for the model in infinite dimensions. The summation over the momentum can be replaced by the integral over the density of state.

Now we have gathered all the assumptions of the dynamical mean field approximation. The goal is to set a scheme to achieve a solution for the self-consistent equation which equate the self-energy of the two models. The method in itself is a generalization of the mean field theory, but unlike the usual mean field theory, say for the Ising model, the mean field here is not a usual order parameter, instead this is a function of the time or frequency. Indeed, there is no explicit order parameter, as no broken symmetry is considered. The ‘order parameter’ now considers the dynamics of the system.

On the other hand, as with a general mean field theory, the spatial fluctuations are completely suppressed. As we will see a major breakthrough of this approximation is to include the spatial dependence systematically into the approximation. The self-consistent condition is valid only at the single particle level, there is no guarantee that high order Green function, such as susceptibility are matched between the two models.

3.3.1 Relation to Single Impurity Problem

With the relationship of the impurity model and the Hubbard model established the Hubbard model in infinite dimensions can now be solved numerically. The self-consistent set of equations are outlined below.

1. Choose an initial $\Sigma(i\omega)$
2. Using Σ calculate $G(i\omega_n)$
3. Find \mathcal{G} using Equation,

$$\mathcal{G}(\mathbf{k}, i\omega) = \frac{1}{G_0^{-1}(\mathbf{k}, i\omega) - \Sigma(\mathbf{k}, i\omega)} \quad (3.22)$$

4. Solve the impurity problem for G
5. Calculate new Σ and return to step 2 until a self-consistent Σ is attained

This loop will return an accurate, in principle exact, solution of the Hubbard model in infinite dimensions. The problem is still not trivial as solving the single impurity problem is a difficult problem. There are a variety of methods to solve this problem each with its own difficulties. There are methods which are exact but scale exponentially with system size such as exact diagonalization. There are statistical methods such as the various flavors of quantum Monte Carlo. Whichever is chosen the solution should enable the calculations of observables which are relevant to the system.

3.3.2 DMFA Results

We will discuss some of the major triumphs of the dynamical mean field theory. The Hubbard model is of such interest in the field of strongly correlated materials due in part to the strength of its predictions. The addition of on site interaction was sufficient to drive a metal to insulator transition for the correct choice of parameters. This transition is observable experimentally most famously in V_2O_3 doped with Cr [50, 51, 52]. The DMFA captures this transition and the quasiparticle features of the system for a wide range of U and T .

The wide range of parameters available for the solution of the Hubbard model has led to the discovery of two critical interaction strengths. The first, labeled U_{c1} signals the transition from metal to insulator. The second labeled U_{c2} a three peak structure appears with a quasiparticle peak at low energies [53]. These findings highlight the richness of the Hubbard model in spite of its apparent simplicity. With these findings there is interest in understanding how the system behaves in lower dimensions where the infinite coordination number approximation is no longer valid.

The findings presented are restricted to a mean field solution due to the lack of momentum dependence in the self-energy. While solving the Hubbard model directly in a finite dimension is beyond the capability of even modern day computation there is the possibility to systematically add back in the momentum dependence. The dynamical cluster approximation does this in a full causal manner.

3.3.3 Continuous Time Quantum Monte Carlo

In the following research in order to solve the single impurity problem the continuous time quantum Monte Carlo, CTQMC, technique was employed. The general idea of the CTQMC is to sample the terms in the diagrammatic expansion. The

statistical sampling of the diagrams enables a calculation of the partition function and therefore the Green function. The CTQMC is an efficient method used to solve impurity problems but there is the necessary consideration of the minus sign problem which is still present in the method. A brief outline of the method follows, for further reference the reader is directed towards the comprehensive review in [54] and the references listed therein.

The fundamental assumption of the CTQMC is that the Hamiltonian can be divided into $H = T + V$. T and V contribute to the kinetic energy and the potential energy respectively. With this the partition function may be written in the path integral formulation in term of the Grassmann variables, ψ and ψ^* .

$$Z = \int \mathcal{D}\psi^* \mathcal{D}\psi e^{-S(\psi^*, \psi)}. \quad (3.23)$$

with the action given as

$$S(\psi^*, \psi) = S_0(\psi^*, \psi) - \int_0^\beta d\tau V(\psi^*(\tau), \psi(\tau)). \quad (3.24)$$

We will focus on the systems with local Hubbard interaction in this thesis, we can write V as

$$V = U \sum_{j=1}^{N_c} [n_{j\uparrow} n_{j\downarrow} - h(n_{j\uparrow} + n_{j\downarrow})]. \quad (3.25)$$

First we shifted the energy by a constant K , thus the partition function becomes

$$S(\psi^*, \psi) = S_0(\psi^*, \psi) - \int_0^\beta d\tau V(\psi^*(\tau), \psi(\tau)) + K/\beta, \quad (3.26)$$

the extra constant K , as it is a constant it won't affect the quantities calculated by weighting average over the partition function. It will serve as a tuning parameter in the Monte Carlo sampling as we will explain in the following.

Writing down the partition function in power series expansion, we have

$$\begin{aligned} Z &= e^{-K} \int_{\eta^*, \eta} e^{-S_0} \sum_{k=0}^{\infty} \left(\frac{K}{\beta} \right)^k \int_0^\beta d\tau_1 \dots \int_0^{\tau_{k-1}} d\tau_k \times \\ &\quad \times \left(1 - \frac{\beta}{K} V(\tau_1) \right) \dots \left(1 - \frac{\beta}{K} V(\tau_k) \right). \end{aligned} \quad (3.27)$$

The interaction term is decoupled by a discrete Stratonovich transformation as originally proposed by Hirsch

$$\left(1 - \frac{\beta}{K}V\right) = \frac{1}{2N_c} \sum_{j=1}^{N_c} \sum_{s_j=\pm 1} e^{\gamma s_j(n_{j\uparrow} - n_{j\downarrow})}, \quad (3.28)$$

where $\cosh \gamma = 1 + \frac{\beta U N_c}{2K}$.

Because of the fermion operator, the decoupling fields can be written in a discrete form. The partition function can be rewritten as

$$\begin{aligned} Z = e^{-K} \int_{\eta^*, \eta} e^{-S_0} \sum_{kj\tau s} \left(\frac{K}{2\beta N_c}\right)^k \times \\ \times e^{\gamma s_1[n_{j_1\uparrow}(\tau_1) - n_{j_1\downarrow}(\tau_1)]} \dots e^{\gamma s_k[n_{j_k\uparrow}(\tau_k) - n_{j_k\downarrow}(\tau_k)]}, \end{aligned} \quad (3.29)$$

The measure of the integral and the summation can be written as

$$\sum_{kj\tau s} = \sum_{k=0}^{\infty} \int_0^{\beta} d\tau_1 \sum_{j_1=1}^{N_c} \sum_{s_1} \dots \int_0^{\tau_{k-1}} d\tau_k \sum_{j_k=1}^{N_c} \sum_{s_k}. \quad (3.30)$$

The fermion degree of freedom can be integrated out completely, as the fermion variables only appear in bilinear form. Together with the Wick theorem for calculating the product of fermion variables, we can write the partition function as

$$Z = \frac{Z_0}{e^K} \sum_{kj\tau s} \left(\frac{K}{2\beta N_c}\right)^k \prod_{\sigma} \det\{\mathcal{G}_{\sigma}^0\} \cdot \det[G_{\sigma}^{\{s_i\}}]^{-1} \quad (3.31)$$

where $G_{\sigma}^{\{s_i\}}$ is the Green's function for a particular set of configurations of auxiliary fields in imaginary time. It can be related to the non-interacting Green's function $\mathcal{G}_{s_i}^0$ by a Dyson's equation:

$$[G_{\sigma}^{\{s_i\}}]^{-1} = [\mathcal{G}_{\sigma}^0]^{-1} e^{\gamma W_{\sigma}^{\{s_i\}}} - e^{\gamma W_{\sigma}^{\{s_i\}}} + \text{I} \quad (3.32)$$

with $W_{\sigma s_i}^{\{s_i\}} = \text{diag}(\sigma s_i)$ and $[\mathcal{G}_{\sigma}^0]_{pq} = \mathcal{G}_{\sigma}^0(j_p, \tau_p; j_q, \tau_q)$ are $k \times k$ matrices.

In order to ensure these conditions this research utilizes a Metropolis algorithm. The Metropolis algorithm proposes a new configuration and either accepts or rejects this with a probability equal to the ratio of the transition matrices. In this way

even the least likely change has a possibility of being accepted and thus ergodicity is fulfilled with the detailed balance condition being fulfilled explicitly.

The diagrams are sampled using a Markov process via the Metropolis algorithm. As long as the sampling space is not sluggish, the Markov process will converge to the expected distribution of diagrams provided the conditions of ergodicity and detailed balance are satisfied. The reason for introducing a constant, K , is to tune the Metropolis dynamics of the sampling. Additionally, in general, the weight of the configurations can be positive or negative. This results in the infamous minus sign problem in quantum Monte Carlo, the average sign can also be tuned by adjusting K .

The minus sign problem is still present within the formulation of the CTQMC. It can be seen as a cancellation problem where each sample comes with a randomly assigned positive or negative weight. The average of the sign of the accepted updates to the configuration describes the so called sign problem. Careful examination of the sign problem is required in order to ensure that the calculations are trustworthy.

For single impurity problem, it can be shown that there is no minus sign problem. For multiple impurities, such as those encountered in the dynamical cluster approximation the minus sign problem is inevitable. It usually gets exponentially worse as a function of inverse temperature, and interaction strength. The value of K may have to be tuned to maintain a delicate balance between the efficiency of sampling and the severity of the minus sign problem.

3.4 Dynamical Cluster Approximation

In order to add in the momentum dependence to the DMFA one possibility is to add in a cluster expansion to the impurity part. This can be seen as a coarse graining step. The DMFA coarse grained the entire Brillouin zone resulting in a local self-

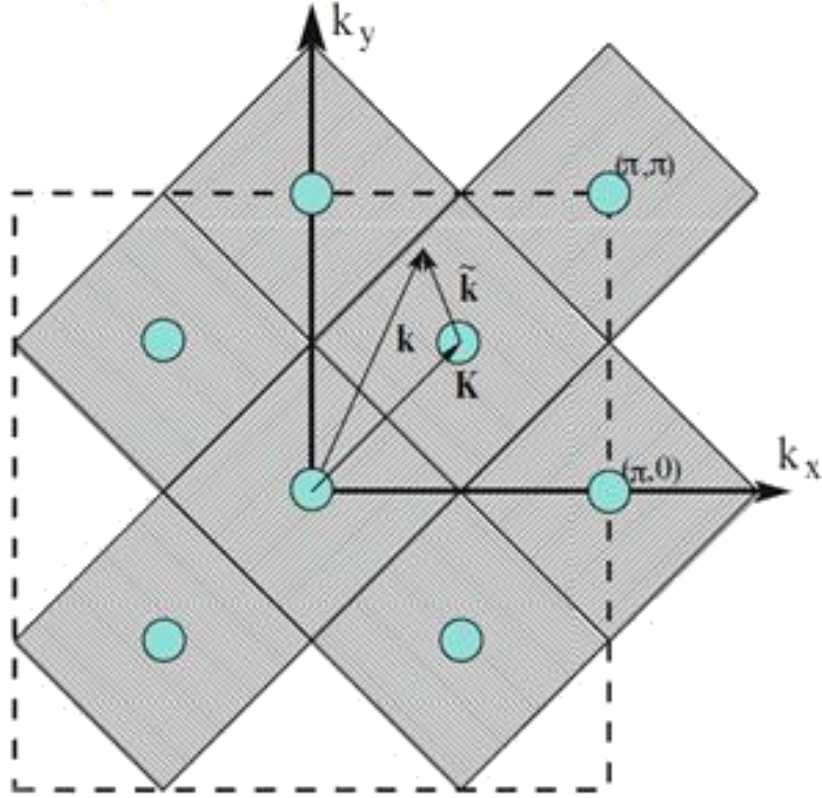


FIGURE 3.1: A two dimensional cluster illustrating tiling of the Brillouin zone. Each momentum point k within the cluster is found via the sum of $K + \tilde{k}$. The self-energy of the points within a cluster are assumed to be weakly momentum dependent and thus may be mapped to a coarse grained value within the cell. Image from [55]

energy. The dynamical cluster approximation, DCA, systematically restores the momentum dependence by including non-local corrections to this quantity. This way the spatial dependence of the system can, to some degree, be studied.

In order to begin the reciprocal lattice is divided into N_c clusters as shown in Fig. 3.1. Each cluster should be identical and of linear size δk . The coarse graining step of the DCA will average the Green function within each cluster. Thus if $N_c = 1$ the DMFA result will be recovered. When $N_c > 1$ correlations of length $\approx \frac{\pi}{\delta k}$ are recovered. Correlations of all lengths could be included in this manner should the computational power be available. While that is clearly not the case there is still much to be gained by the inclusion of even a small number of cluster sites.

In the DCA each cluster is represented by a momentum \mathbf{K} at the center of the cluster. Thus instead of a momentum independent approximation the self-energy is approximated by

$$\Sigma(\mathbf{K} + \tilde{\mathbf{k}}, \omega) \simeq \Sigma(\mathbf{K}, \omega), \quad (3.33)$$

where \mathbf{K} is the momentum of the center of a cluster site, and $\mathbf{K} + \tilde{\mathbf{k}}$ is the momentum of a patch of the Brillouin zone, see fig. 3.1. The underlying assumption is that the self-energy is only weakly momentum dependent. This self-energy feeds into the coarse grained Green function. Each Green function in the Feynman diagrams should therefore be replaced by a coarse grained Green function. This coarse grained Green function,

$$\bar{G}(\mathbf{K}) \equiv \frac{N_c}{N} \sum_{\tilde{\mathbf{k}}} G(\mathbf{K} + \tilde{\mathbf{k}}), \quad (3.34)$$

with N the number of points in the lattice and the summation running over all k points in the cluster. In this way the diagrams are unchanged by the problem and the complexity is greatly reduced as $N_c \ll N$.

This method attempts to preserve the translational symmetry of the lattice. This occurs through the coarse graining over the sites within the cluster. Through this procedure the DCA restores the momentum conservation of the lattice within the accuracy of the cluster size. This can be seen as considering the Laue function

$$\Delta(k_1, k_2, k_3, k_4) = \sum_r \exp(i(k_1 - k_2 + k_3 - k_4) \cdot r), \quad (3.35)$$

for momentum conservation, the summation can be evaluated as a delta function which represent two incoming particles (with momenta k_1 and k_3) and two outgoing particles (with momenta k_2 and k_4).

$$\Delta(k_1, k_2, k_3, k_4) = N \delta_{k_1+k_3, k_2+k_4}, \quad (3.36)$$

where N is the total number of points in the first Brillouin zone. The DCA maps the momentum k to momentum $M(k)$, where it can be any value within a cluster.

The Laue function becomes

$$\Delta_{DCA}(k_1, k_2, k_3, k_4) = N_c \delta_{M(k_1)+M(k_3), M(k_2)+M(k_4)} \quad (3.37)$$

$$= \Delta(k_1, k_2, k_3, k_4) + \mathcal{O}(\delta k), \quad (3.38)$$

where N_c is the number of the clusters, that is the number of discrete non-overlapping patches in the Brillouin zone. A basic assumption of the DCA is that the self-energy is only weakly momentum dependent. As such, the approximation shown in equation 3.33 should hold.

From the above argument, one can see that the conservation of momentum which is completely neglected in the dynamical mean field theory is partially restored. In particular, the conservation of momentum for the two particle vertex is restored with the error which is proportional to the linear size of the cluster, $\delta k = 2\pi/N_c^{1/D}$, where D is the spatial dimension of the system

Therefore, the dynamical cluster approximation can systematically restore the conservation of momentum by increasing the cluster size. The next step is to devise a scheme to determine the self-energy.

The self-consistent loop is much the same as the DMFA with the additional step of coarse graining. In this way the DCA is a natural evolution from the DMFA. The inclusion of the spatial correlations gives rise to the possibility to analyze local physics.

The calculation of the self-energy of the DCA follows a similar procedure to that outlined for the DMFA. The major difference is that the self-energy carries the momentum dependence and the allowed momentum points are based on the momentum of each cluster.

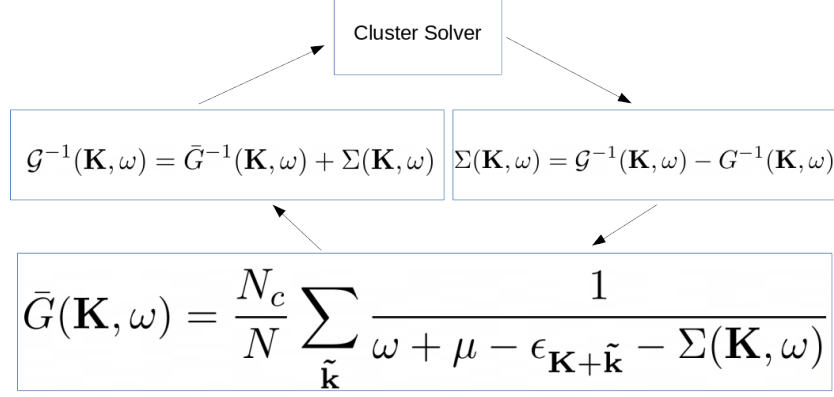


FIGURE 3.2: The dynamical cluster approximation self-consistency loop. The coarse-graining procedure shown in steps 1 and 2 highlights how the degrees of freedom are reduced from an intractably complex problem to a more manageable size through the neglect of momenta within the cluster cell.

In contrast of the dynamical mean field theory, there is the step of coarse graining over all momentum points within a cluster.

$$\bar{G}(\mathbf{K}, \omega) = \frac{N_c}{N} \sum_{\tilde{\mathbf{k}}} \frac{1}{G_0^{-1}(\mathbf{K} + \tilde{\mathbf{k}}, \omega) - \Sigma(\mathbf{K}, \omega)} \quad (3.39)$$

This is then related to the bare cluster Green function through the same relation as that for the dynamical mean field theory, except the bare Cluster Green function, the lattice Green function and the self energy all carry momentum dependence.

$$\mathcal{G}(\mathbf{K}, \omega) = [\bar{G}^{-1}(\mathbf{K}, \omega) + \Sigma(\mathbf{K}, \omega)]^{-1}. \quad (3.40)$$

This bare Green function can then be fed into a cluster solver which will produce a new cluster Green function. This is then used to recalculate the self-energy. The current DCA iteration compares the self-energy its value with the previous iteration. The basic outline of the algorithm is presented in Fig. 3.2.

For any practical numerical calculation, the cluster is limited to rather small size. This is due to the limitation of solver for solving many impurities problems.

The algorithm becomes very numerical heavy as the impurity cluster solver scales poorly with the number of impurities. Moreover the minus sign problem also occurs

in the quantum Monte Carlo quite severely. For almost all practical calculations, the cluster size is limited to about 10 to 20 sites. We list the algorithm of the dynamical mean field theory here.

1. Choose an initial $\Sigma(\omega)$
2. Using Σ calculate $G(i\omega_n)$
3. Find \mathcal{G} using Equation

$$\mathcal{G}(\mathbf{K}, \omega) = [\bar{G}^{-1}(\mathbf{K}, \omega) + \Sigma(\mathbf{K}, \omega)]^{-1}. \quad (3.41)$$

4. Solve the impurity cluster problem by QMC.
5. Calculating the lattice Green function by the coarse-graining procedure.

$$\bar{G}(\mathbf{K}, \omega) = \frac{N_c}{N} \sum_{\tilde{\mathbf{k}}} \frac{1}{G_0^{-1}(\mathbf{K} + \tilde{\mathbf{k}}, \omega) - \Sigma(\mathbf{K}, \omega)} \quad (3.42)$$

6. Calculate new Σ and return to step 2 until a self-consistent Σ is attained

The momentum information gathers the possibility of calculating susceptibilities which rely upon location resolution such as the antiferromagnetic susceptibility. The DCA is also responsible for the generation of other notable observables and quantum critical features.

Chapter 4

Non-Fermi Liquid and Quantum Critical Point

The methods discussed enable the investigation of the Hubbard model. An initial decision to be made is the number of nearest neighbors to include. Through the number of nearest neighbors the dimensionality is decided. The phases of the two dimensional Hubbard model and the infinite dimensional Hubbard model have been investigated [56, 57] previously. They demonstrate quantum critical points at differing fillings. This thesis then investigates the behavior of the three dimensional Hubbard model as a means to identify what occurs in intermediate dimensions to the quantum critical point.

4.1 Findings in Two Dimensions

The phases of the two dimensional Hubbard model seen in Fig. 4.1 demonstrate a change in behavior of the system as doping is decreased. The figure shows the quasiparticle weight of the system at various fillings and temperatures. For this particular model the interaction strength is $U = .75W$, where W is the bandwidth. The figure demonstrates the qualitative difference of the low temperature behavior as the system approaches half-filling. There is both a Fermi liquid like phase and a non-Fermi liquid like phase.

In order to identify different phases the quasiparticle weight is analyzed. The imaginary time self-energy is used to find the quasiparticle weight, Z . The quasiparticle weight is the ratio of the reduced mass of the electron in a system to the normal mass of the electron, $\frac{m^*}{m}$. Since the reduced mass is less than the mass of an electron the quasiparticle weight can only take on values between 0 and 1. In a NFL the quasiparticle weight should vanish by 0 temperature. A Fermi liquid is expected to maintain a finite value as the temperature approaches $0k$. The behavior

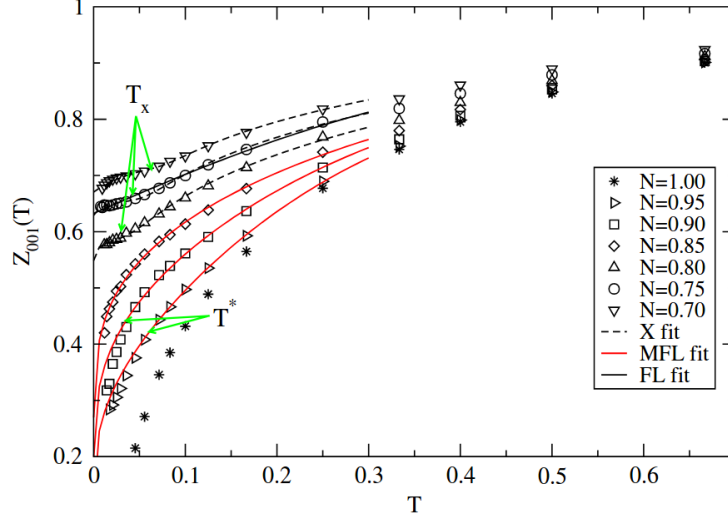


FIGURE 4.1: Quasiparticle weight of the lowest Matsubara frequency ν temperature. Here $U=\frac{3}{4}$ bandwidth of 2D tight binding. The lines are fits of the data to various forms of the quasiparticle weight. The values T_x are found via fitting the crossover form of self energy to the data. The T^* values are found using the peak in the χ'' . There is a clear separation between FL behavior and NFL behavior. [56]

of the quasiparticle weight at low temperatures should be sufficient to distinguish between these two states.

In addition to showing the different phases at low temperature the Hubbard model shows that there is a intermediate phase at higher temperature. In the higher temperatures the system behaves as a marginal Fermi liquid (MFL). A marginal Fermi liquid has a real frequency self-energy whose imaginary part takes the asymptotic form

$$\text{Im}[\Sigma_{MFL}(\omega)] \propto \max(\omega, T). \quad (4.1)$$

This contrasts with the Fermi liquid form which is proportional to T^2 ,

$$\text{Im}[\Sigma_{FL}(\omega)] \propto \max(\omega^2, T^2). \quad (4.2)$$

In the figure above the transition from the MFL to the FL phases are identified by the crossover temperature, T_x . This temperature decreases as the filling increases. This temperature is identified via a fitting parameter.

The functional forms of the self-energy shown in [58] can be transformed to imaginary time via the Kramers-Kronig relation,

$$\Sigma(i\omega_n) = - \int \frac{d\omega}{\pi} \frac{Im[\Sigma(\omega)]}{i\omega_n - \omega}. \quad (4.3)$$

The form of the marginal Fermi liquid has the form

$$\frac{Im\Sigma_{MFL}(i\omega_0)}{\omega_0} = \frac{\alpha}{\pi} \left[\ln \left(\frac{(\pi^2 + 1)T^2}{\pi^2 T^2 + \omega_c^2} \right) - \frac{2}{\pi} \tan^{-1} \frac{1}{\pi} \right]. \quad (4.4)$$

Here α is a fitting constant and the cutoff ω_c is on the order of the bandwidth W .

By way of contrast, for the Fermi liquid self-energy imaginary part is defined as

$$\frac{Im\Sigma_{FL}(i\omega_0)}{\omega_0} = \frac{-2\alpha T}{\pi} \left(\frac{\omega_c}{T} + 0.066235 - \pi \tan^{-1} \frac{\omega_c}{\pi T} \right). \quad (4.5)$$

Identifying the temperature at which the phase crosses over from one to the other can be constructed using the same integrals [56]. The crossover form is obtained by assuming that the self-energy below energy ω_x or temperature T_x is given by the Fermi liquid form and it is given by the marginal Fermi liquid form otherwise.

This crossover form is given by

$$\begin{aligned} \frac{Im\Sigma(i\omega_0)}{\omega_0} = & \frac{-2\alpha T}{\pi} \Theta(T_x - T) \left[\frac{\omega_x}{T} + 0.066235 - (0.308 \frac{\omega_x}{\pi T} \right. \\ & \left. + \pi \tan^{-1} \frac{\omega_x}{\pi T}) - \frac{\omega_x}{T} \ln \left(\frac{\omega_x^2 + \pi^2 T^2}{(1 + \pi^2) T^2} \right) \right] + \omega_x [0.0981 + \frac{1}{2} \ln(\frac{\omega_c^2 + \pi^2 T^2}{(1 + \pi^2) T^2})]. \end{aligned} \quad (4.6)$$

The parameters $\alpha, \omega_c, T_x, \omega_x$ are determined via a non-linear fitting routine. The crossover temperature is found to be 0 at the critical filling of $N = 0.85$ for the case of the two dimensional Hubbard model.

The transition from MFL to NFL is found by identifying the emergence of a pseudogap. This can be seen through the peak in the $Q = 0$ value of the spin susceptibility as temperature is decreased. The temperature at which the pseudogap emerges is labeled T^* . This temperature decreases as the doping increases from half-filling.

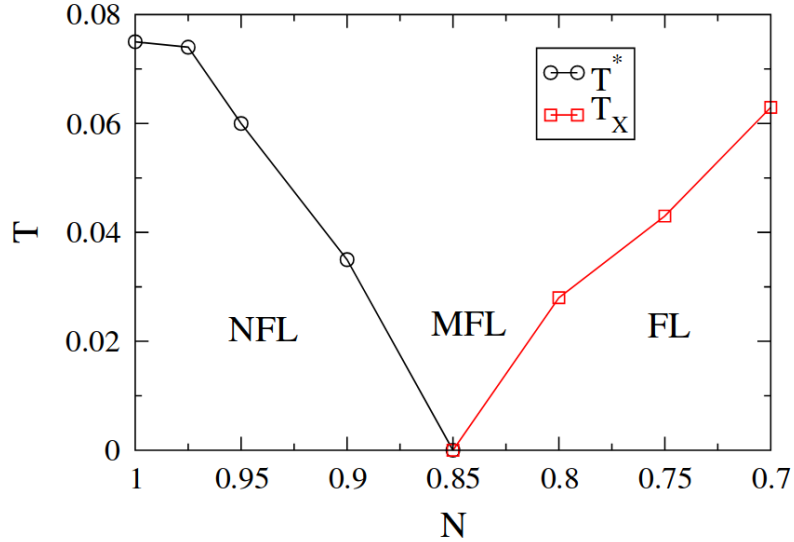


FIGURE 4.2: Phase diagram of the two dimensional Hubbard model. The figure illustrates quantum critical wedge. The critical filling of $N=0.85$ is seen by $T_x = 0K$ [56]

The temperature where the system transitions from a MFL to either a NFL or a FL of the 2D Hubbard form a phase diagram as seen in Fig. 4.2. The transition temperature results in a wedge shaped phase diagram with the filling being the relevant parameter. This is indicative of a quantum critical point. Indeed to numerical accuracy the filling $N = 0.85$ shows a crossover temperature of $0K$ indicating that there is indeed a quantum critical point at a finite doping.

4.2 Current Work

This research aims to show that there is similar evidence of quantum criticality for the Hubbard model in three dimensions. Utilizing the continuous time quantum Monte Carlo in conjunction with the DCA calculations for the quasiparticle weight shows separate phases as the system approaches half-filling.

This work uses a 16 site 3D Betts cluster [59] for the DCA algorithm. The interaction is set to $U = 0.75W$ where W is the bandwidth of the non-interacting system. The temperature ranges currently studied vary from $\beta = 2-80$. The largest β were chosen due to time constraints on the super computer. These simulations

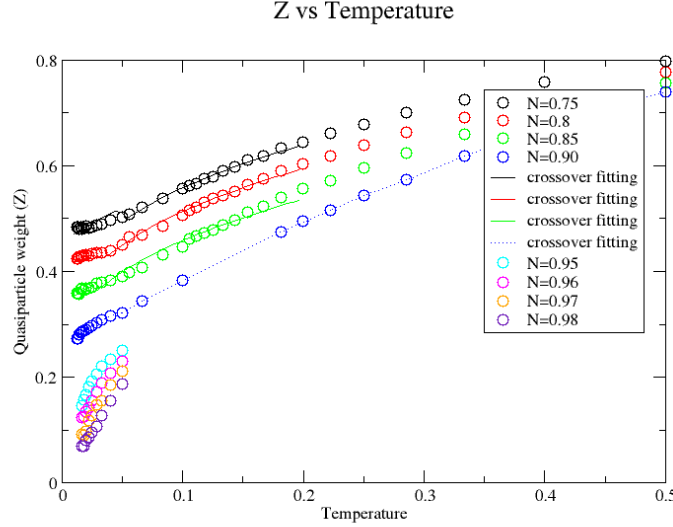


FIGURE 4.3: Various fillings for the quasiparticle weight of the 3D Hubbard model. Dopings farther removed from half filling saturate to a finite value at low temperatures. Beginning at $N = 0.95$ the quasiparticle weight fails to saturate as temperature decreases. This demonstrates the separation between Fermi liquid behavior and non-Fermi liquid behavior at a finite filling. The crossover fitting line is shown for the dopings above $N = 0.95$

demonstrate the separation of two phases at an finite doping following a similar path to the two dimensional system.

In order to extract the quasi-particle weight, we have to set the relation between the self-energy and the quasi-particle weight, as self-energy is readily available in the DCA.

The quasi-particle weight is related to the retarded self energy,

$$Z_{\mathbf{k}} = \frac{1}{1 - \partial_{\omega} \text{Re}[\Sigma^R(\mathbf{k}, \omega)]|_{\omega=0}}. \quad (4.7)$$

The result of the DCA is given in Matsubara frequency. In order to relate the real part of the retarded self-energy to the Matsubara self-energy we use

$$\begin{aligned} \left. \frac{\partial \text{Re}[\Sigma(\mathbf{k}, \omega)]}{\partial \omega} \right|_{\omega=0} &= \int \frac{d\omega' \text{Im}[\Sigma(\mathbf{k}, \omega')]}{\pi \omega'^2} \\ &= \left. \frac{\text{Im}[\Sigma(\mathbf{k}, i\omega_n)]}{\omega_n} \right|_{\omega_n \rightarrow 0}. \end{aligned} \quad (4.8)$$

The first line is obtained by taking the derivative with respect to the ω on the Kramers-Kronig relation and the second line is from the analytic continuation,

$$\Sigma(\mathbf{k}, i\omega_n) = \int \frac{d\omega' \text{Im}[\Sigma(\mathbf{k}, \omega')]}{\pi(\omega' - i\omega_n)} \quad (4.9)$$

Thus the quasi-particle weight can be calculated without analytic continuation by the equation

$$Z_{\mathbf{k}} \approx \frac{1}{1 - \text{Im}[\Sigma(\mathbf{k}, i\omega_0)]/\omega_0}. \quad (4.10)$$

In order to find the quasiparticle weight of the system it is important to identify the Fermi surface. This is achieved through interpolation of the self-energy. The value of the self-energy is interpolated via inverse distance weighting [60]. This allows for information from all available points to contribute to the interpolated value such that the closest have a much stronger weighting than the further points. The interpolation follows the formula

$$f(x) = \begin{cases} \frac{\sum_i w_i(x) u_i}{\sum_i w_i(x)}, & d(x, x_i) \neq 0 \text{ for all } i \\ u_i, & d(x_i, x) = 0 \text{ for some point } i. \end{cases} \quad (4.11)$$

Where i sums over all known points, u_i is the functions value at the known points, the values x, x_i are the location of the interpolated point and the known points respectively, $d(x, x_i)$ is the distance of the interpolated point to the known point, and w_i is the weighting function given to each point. The weighting function is defined by

$$w_i(x) = \frac{1}{d(x, x_i)^p} \quad (4.12)$$

where p is a parameter chosen to control the rate with which the weight drops off over distance. In this research a value of 6 was found to be ideal for p . The self-energy is then used to find the Green function and that in turn gives the momentum distribution, $n(q)$. The $\max\left(\left|\frac{dn(q)}{dx}\right|\right)$ identifies the k point at which

the Fermi surface occurs. This k point is then used for the calculation of the quasiparticle weight.

The three dimensional Hubbard model quasiparticle weight shows a similar separation between the quasiparticle weights to that seen in the two dimensional system. The transition doping is much closer to half-filling. The results included in Fig. 4.3 show a clear separation at a finite filling between FL and NFL behavior. The simulation is run to the temperature of $\beta = 80$ below which the computational cost becomes prohibitively expensive. Beginning at $N = 0.95$ the quasiparticle weight tends towards 0 as the temperature decreases. The three dimensional results contrast with the two dimensional case the NFL region begins at $N = 0.85$. Three dimensions appears to push the critical filling nearer to half filling.

In Fig. 4.4 the crossover temperature is plotted for the dopings show in Fig. 4.3. The crossover form is fit by a non-linear regression given in equation 4.6. In order to avoid numerical errors within the fitting routine the step function Θ is replaced with the approximate function

$$\Theta(x) \approx \frac{1}{2} + \frac{1}{2} \tanh(kx). \quad (4.13)$$

This function approaches the form of the step function as $k \rightarrow \infty$ whose value at 0 is 0.5. For the purposes of the fitting the value of k is chosen to be 1000. The figure follows a approximately linearly decreasing form. The findings imply that the crossover temperature would be 0 at a finite doping. Below this doping the system would cease to be in a Fermi liquid state at any temperature. When the system's doping is below this critical doping the system would likely enter some non-Fermi liquid state at some low temperature. The decrease indicates that the crossover temperature will be 0K for the approximate filling of $N = 0.95$. This matches filling at which a NFL character emerges in the quasiparticle weight.

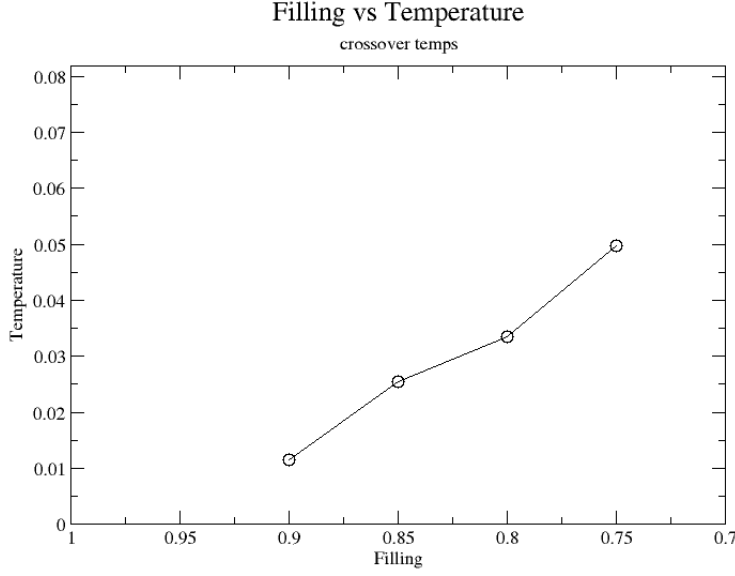


FIGURE 4.4: The monotonic decrease of the crossover temperature verses doping. As the doping approaches half-filling the crossover temperature decreases to $0K$. Following the general idea of the quantum critical point. It seems to point towards a critical filling of $N = 0.95$

There is evidence that the non-Fermi liquid state is a pseudogap state. This can be seen in viewing the spectra of the system. The Green function data of the low doping cases are analytically continued to find the spectra. In Fig. 4.5 the analytically continued spectra for $N = 0.95$ show evidence of a pseudogap emerging. These values were found by employing the maximum entropy method. The pseudogap begins to develop around $\beta = 40$ and appears fully developed by $\beta = 70$. The emergence of the pseudogap roughly coincides with a maxima in the cluster spin susceptibility. The cluster spin susceptibility seen in Fig. 4.6 does not conclusively show a maxima at a finite temperature. Ideally the shape of the data would follow the form where it would increase until a finite temperature below which it would begin a monotonic decrease. This general form is present at all dopings though the noise is sufficient that no conclusions about the temperature where the susceptibility is maximum can be drawn at the present time.

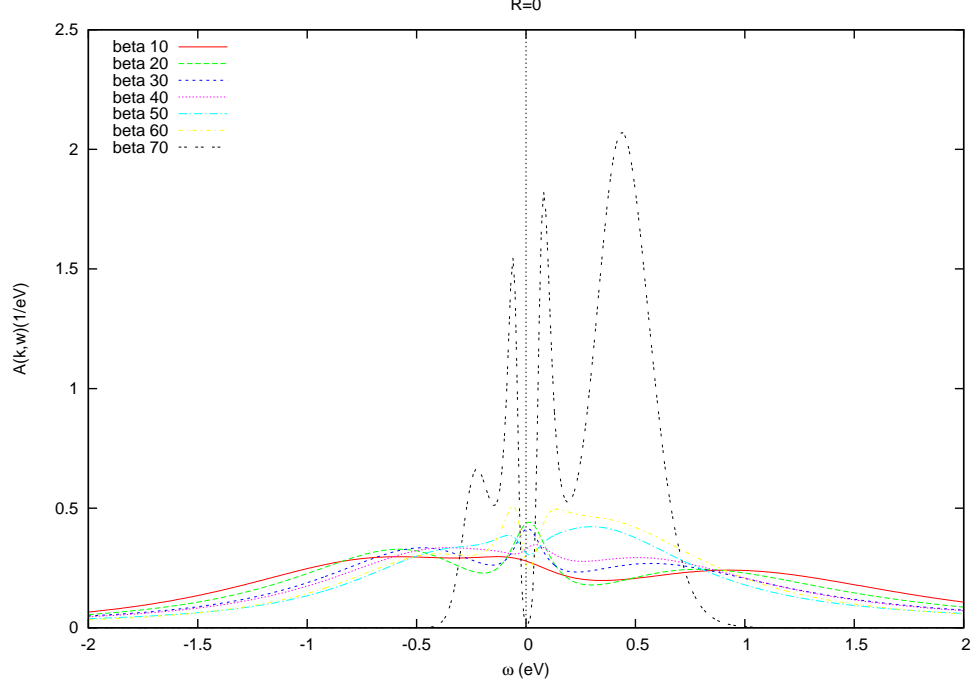


FIGURE 4.5: The spectra at different β for the filling of $N = 0.95$. The pseudogap begins to emerge at $\beta = 40$. As the temperature decreases the pseudogap become more pronounced.

Removing the noise in the susceptibility calculations has proven difficult. The source of the noise is uncertain though there are the common culprits of insufficient Monte Carlo measurements, insufficient self-consistency, or a bad model. These can all be remedied with orders of magnitude more computational time but they are currently out of reach with the given resources available. It is possible that this follows the general form seen in the two dimensional Hubbard model where the maxima in the susceptibility coincides with the emergence of the pseudogap state. That is the hypothesis of this researcher though further efforts are required to definitively show this to be the case.

The main conclusion from the DCA analysis of the three dimensional Hubbard model is that we find evidence of marginal Fermi liquid. We are able to extract the crossover temperature between the Fermi liquid at low temperature and the marginal Fermi liquid at high temperature. The natural explanation of the marginal

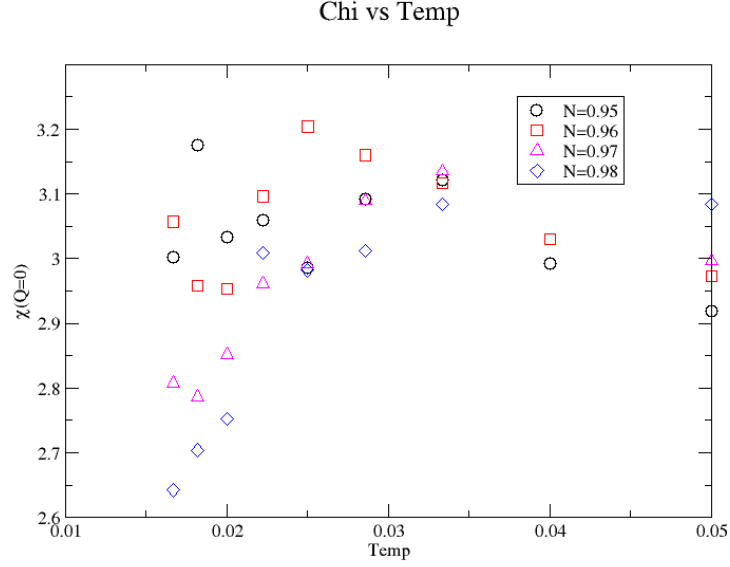


FIGURE 4.6: The cluster susceptibility of the 3D Hubbard model. Currently the noise is too high to properly determine a maximum. The general form of a maximum value between the extreme high and low temperatures is seen and is more pronounced for the fillings $N = 0.97$ and $N = 0.98$

Fermi liquid is the existence of the quantum critical point and that the marginal Fermi liquid is the consequence of the quantum criticality at finite temperature. We attempt to locate the pseudo-gap temperature by analysing the spin susceptibility, however the data is rather noisy and we are not able to locate the pseudo-gap temperature at the moment.

Chapter 5

HPX Implementation of the Parquet Algorithm

In this chapter, the work of improving network performance of the HPX implementation of the parquet approximation is presented. This work was done in collaboration with Bibek Wagle, Ka-Ming Tam, Mark Jarrel, Hartmut Kaiser, and Juana Moreno. The material has been published in 2018 IEEE [61]. My contribution to this research involved implementing the relevant physics equations in C++, identifying and aiding with the implementation of areas where the task based implementation could improve the simulations efficiency, and optimising data distribution across a highly distributed simulation. B. Wagle, S. Kellar, A. Serio and H. Kaiser, “Methodology for Adaptive Active Message Coalescing in Task Based Runtime Systems,” 2018 IEEE International Parallel and Distributed Processing Symposium Workshops (IPDPSW), Vancouver, BC, Canada, 2018, pp. 1133-1140.

5.1 Motivation

An alternative approach to modeling strongly correlated systems is solving the Hamiltonian via an expansion of Feynman diagrams. This approach avoids the limitations of the numerically exact models which suffer from exponential scaling. Problems which arise due to the minus sign problem and exponential scaling of exact diagonalization inhibit the ability to scale to arbitrarily large problem sizes. This limitation can possibly be circumvented by incorporating perturbative methods. One such method is the parquet approach.

The parquet approach was developed in the 1950’s by Martins [62]. At that time the numerical and memory requirements exceeded the capabilities of the contemporary computers. With the development of larger memory allocations and the exponential speedup of the computational resources have allowed for the applica-

tion of this method. The algebraic scaling of this method make it an ideal candidate to larger scaling runs to solve larger problem sizes.

The parquet method is a self-consistent Feynman perturbation which scales to the third power of the number of frequency and momentum points in memory. As such the simulations rapidly exceed the real time storage capabilities of a single desktop. It requires the computational capabilities of high performance computers. The computational cost scales as the fourth power of the momentum-frequency points due to the inclusion of a large number of matrix inversions. This scaling while costly improves upon the exponential scaling of other numerically exact methods.

In an effort to improve the efficiency of computational simulations HPX [63] was employed to the Parquet algorithm. This effort focused on improving efficiency through utilization of a task based runtime. While the efforts only managed minimal success the effort and results bare documentation. As such this is included in the report.

5.2 Parquet Formalism

The parquet approach was initially developed in the 1950's by Dominicis and Martin. This approach found applications in x-ray absorption and emission [64]. Additionally, it has been used to study the Fermi liquid in a strong magnetic field [65] and the disordered electron gas in a strong transverse magnetic field [66]. These applications with others demonstrate the utility of the parquet approach though the full parquet equations are not often used due to their complexity.

The parquet approach to many body perturbation theory incorporates a large number of two particle diagrams into the calculations. These diagrams, called vertex diagrams, add to the single particle diagrams. They describe the scattering of two particles from an initial state composed of momentum and frequency quantum

numbers to final states. When momentum and energy conservation is enforced only three states are required to determine the entire scattering process. The fourth is determined via the conservation laws. The topology of these diagrams is divided into categories determined by whether they can be decomposed into combination of vertices or not. A reducible vertex is one such that the vertex can be cut into a combination of two vertices by breaking a single green function line in the diagram. The irreducible diagrams are those which cannot be separated without cutting two Green function lines. The fully irreducible vertices are those which require breaking more Green functions to divide them into separate vertices.

The scattering diagrams are separable into particle-particle and particle-hole channels. In the spin basis these channels are divided into four separate channels; singlet, triplet, density, and magnetic. The parquet step forms a relation between the vertices in the different channels. Thus the vertex values are updated based on the other channels. When a self-consistent result is reached the solution can be considered to be two particle self-consistent. Including these values gives the opportunity to achieve more physical results at the cost of higher computational complexity and a larger requirement for storage in the numeric simulation. In order to fully realize the capabilities of such an algorithm the high costs must be mitigated so that the simulation may complete in an efficient manner.

The parquet formalism follows a self-consistent loop. It is outlined in Fig. 5.1. The steps of the algorithm are outlined here.

1. Calculate the bare susceptibility χ_0 as the product of two green functions
2. Calculate the full vertex, F from χ_0 using the Bethe-Salpeter equation
3. Update the irreducible vertices through the parquet step
4. Calculate a new full vertex using the updated irreducible vertices

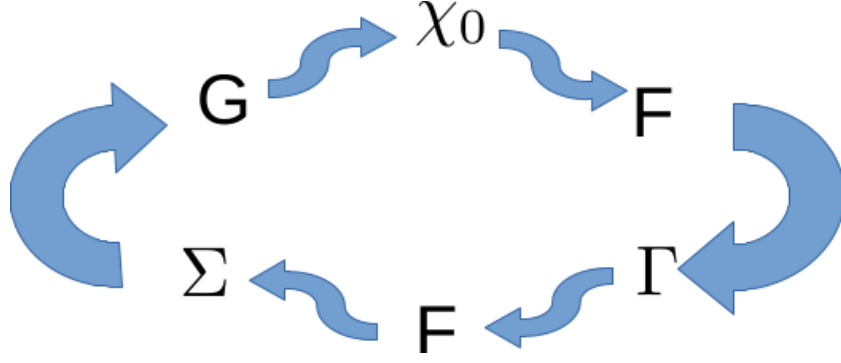


FIGURE 5.1: The self-consistent loop of the parquet algorithm. The parquet step where the irreducible vertices, Γ , are found from the full vertex, F , requires the communication of many small packets of information through the distributed memory of the computational environment.

5. Calculate the self-energy via the Schwinger-Dyson equation
6. Find the Green function from the Dyson equation

The titular parquet step involves gathering values of from disparate portions of the distributed memory in order recalculate vertex values. Computationally speaking this requires gathering small bits of data for each vertex value. As the simulation size exceeds the storage capabilities of a single machine the data is distributed across many compute nodes. Gathering data from the different compute nodes requires utilizing the network which is significantly slower than the compute speeds on node. Since this must be done for all the irreducible vertices the strain on the network is not small. This can be a significant bottleneck for the computation. This study also investigates the improvement of the parquet application through the use of HPX.

5.3 Introduction of HPX

Exascale computing with tens of thousands of nodes solving complex scientific problems simultaneously call for task based runtime systems. A task based runtime system involves decomposing an algorithm into small units of work to be executed with very little overhead. These units of work are known as tasks. In such a large

computing environment tasks based systems are a practical replacement for MPI [67]. Simulations run in a high performance system require communication between the many computational nodes.

The effects of the task based system depend upon the simulation employed. As the system becomes more and more complex the messaging of MPI should prove a poorer and poorer mechanism as the efficiencies of such a system depend wholly upon the slowest node. These problems are costly to overcome and require significant amounts of designer time which can be understood to be the most valuable resource of all. A task based system should leverage the entire system with minimal intervention of the designer. Thus the expected improvement should be significant.

The latency of the system determines the time a simulation requires. There is also the consideration of the overhead with communication between the nodes. These factors determine whether a system is network bound or computationally bound. This in turn determines how best to improve the efficiency of the simulation. The inefficiencies should be removed. These inefficiencies such as waiting time for network communication to complete can be improved upon via the coalescing of messages.

Efficient communication between computational resources of the cluster is largely dependent on latency and the bandwidth of the network as well as the overheads associated with the creating and sending of messages [68]. Network overheads can be cumulative when they occur in rapid succession. The result is strain on the network of the system which can be mitigated through adjusting the rate of the messages. In the context of a task based runtime system, where fine grained communication is ubiquitous, efficient use of network bandwidth and reduction of overheads introduced by the transmission of information is vital. These improvements are certain

to decrease the runtime of the simulation and as such these improvements should show a immediate benefits with marginal cost to development time.

Aggregating messages to improve communication across a network is not a new idea. This may be done manually but as previously mentioned the cost is significant in terms of developer time. This coalescing would be improved if the automation of this led to an improvement of the simulations without any developer intervention. The goal of this is to include parameters which optionally engaged enable this automation so that the network communication improves automatically.

The combination of network information from small individual packets and sending them as a larger message, as in Fig. 5.2, is an optimization technique that has been in use for quite some time now [69]. This so called coalescing of messages effectively sends the same amount of data by postponing the communication until many messages can be sent simultaneously. At the same time this keeps the per message overheads at a minimum. Although programmers can manually coalesce messages to optimize their applications, this is a costly effort and one that is dependent not only on the simulation but also the system running it. As such coalescing is practical only in small and simple applications. Recent work such as Active Pebbles [70], AM++ [71] and Charm++ [72], have implemented some form of message coalescing solutions provided by runtime systems. Such solutions are largely beneficial in terms of reducing program complexity and coding time. A programmer would simply enable message coalescing and the runtime would intelligently coalesce messages bound to the same destination.

One caveat of this approach is determining how many messages to coalesce in a single message. A single message can be defined by either the size of the buffer, number of messages or a timeout. Since each application has different communication patterns, a single parameter that works best for all conceivable applications

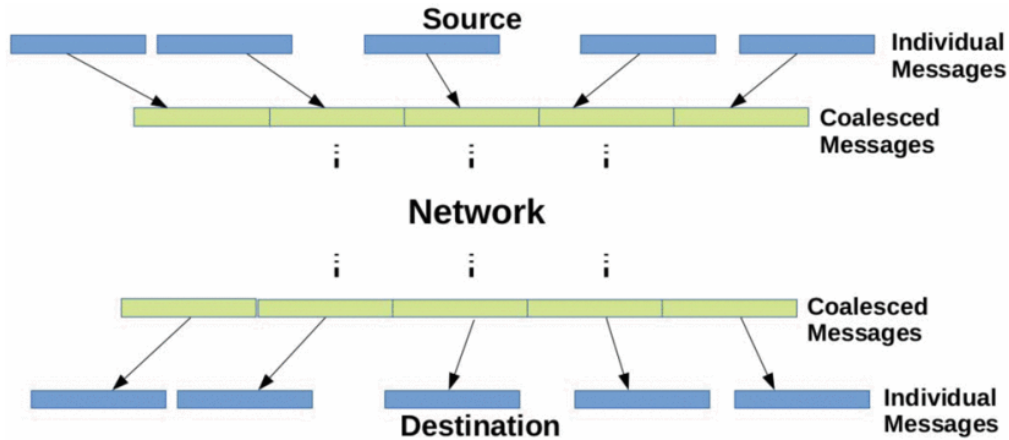


FIGURE 5.2: A diagrammatic representation of message coalescing. Individual active messages are grouped together to form a large message at the sending end and which is reconstructed into the original individual entities at the receiving end.

simply does not exist. Furthermore, there may be phases in an application where communication is heavy and heavy coalescing would be beneficial, juxtaposed with periods of time when communication is light and sparse that would benefit from different parameters for coalescing. An intelligent adaptive message coalescing approach that dynamically varies its parameters depending upon the application's behavior would be useful.

Recent research [72] has successfully demonstrated a basic adaptive approach for message coalescing where different sets of parameters for coalescing are tried during each iterative step on an all-to-all benchmark using PICS: A Performance-

The messaging system depends upon the communication pattern employed by the simulation. Requiring the developer to manually indicate when to coalesce messages and how often is a enterprise ripe with error and once again using valuable time which could be used on more productive alternatives. There are times when the bottlenecks are unknown to the developer at runtime. Instead of requiring a time taking and laborious optimisation step it would be beneficial if the application could automate this. In an effort to progress towards this optimization the current research is presented.

Analysis-Based Introspective Control System [73]. PICS converged to a decision on coalescing buffer size in 5 decisions. This could be improved upon by creating an advanced adaptive framework able to monitor in real time the network overhead due to fine grained communications. It could select efficient message coalescing parameters based upon that information. Such a system would be able to intelligently vary coalescing parameters based on the phase of the application and would provide a general solution to adaptive message coalescing for applications that do not have a well defined iterative step or a predictable pattern of communication.

HPX [63] is a task based runtime system with real time performance monitoring and tuning capabilities that makes it an obvious choice for experimentation. In order to achieve advanced adaptive message coalescing in HPX, the following steps need to be completed: (i) Implementation of message coalescing in HPX, (ii) Identification of metrics and runtime characteristics that relate to the network overhead associated with fine grained communication, and (iii) Utilization of the identified metrics for adaptive tuning of coalescing for scientific applications. This work presents the first two steps towards the overall goal of achieving automated message coalescing.

As mentioned previously, other task based runtime systems have the ability to coalesce messages. These include Active Pebbles [70], AM++ [71] and Charm++ [72]. Our implementation of message coalescing differs from these implementations in a few fundamental ways. Currently, Active Pebbles, AM++ and Charm++ use buffer size as a means of controlling the granularity of communication. A buffer is allocated and once filled the message is sent. Our approach, however, is to control the number of individual messages to coalesce. Determining when to override messaging coalescing parameters is another important distinction in methodology. While Active Pebbles and AM++ normally send a message when

the buffer is full, they also support a flush method which immediately sends the message regardless of the amount of information in it. Charm++ has a periodic check mechanism which performs an immediate send if no messages were sent between subsequent checks. Our implementation of message coalescing allows the coalesced message to be sent after a timeout. When the first message enters the coalescing queue, a timer is set which flushes the coalescing queue on expiration of the timer. Hence, each instance of coalesced messages is sent out either when the coalescing queue is full or when the timeout is triggered. These strategies are necessary to prevent deadlocks caused by unsent messages due to an insufficient amount of data or an insufficient number of messages waiting to be sent.

5.4 HPX Runtime System

HPX is a C++ runtime system based on the solid theoretical foundation of the ParalleX [74] model. It exposes a concurrency and parallelism API that is consistent with the current ISO C++ standard. HPX parallel applications can run on both a single machine as well as a cluster with hundreds of thousands of nodes. It is an alternative to the more traditional programming paradigms such as MPI [67]. The architecture of HPX is shown in Fig. 5.3. The HPX threading system employs lightweight tasks, known as HPX threads, that are scheduled on top of operating system threads. A locality in HPX is an abstraction for a physical node. The Active Global Address Space (AGAS) system in HPX provides a mechanism for addressing any HPX object globally. Each object in HPX is assigned a Global Identifier (GID) that is maintained throughout the lifetime of the object even if it is moved between nodes in the system. Local Control Objects (LCOs) are used to synchronize tasks generated by the application. The parcel subsystem is responsible for executing a task remotely and the Performance Counter Framework is used for instrumentation purposes. Additional information on HPX can be found in [63].

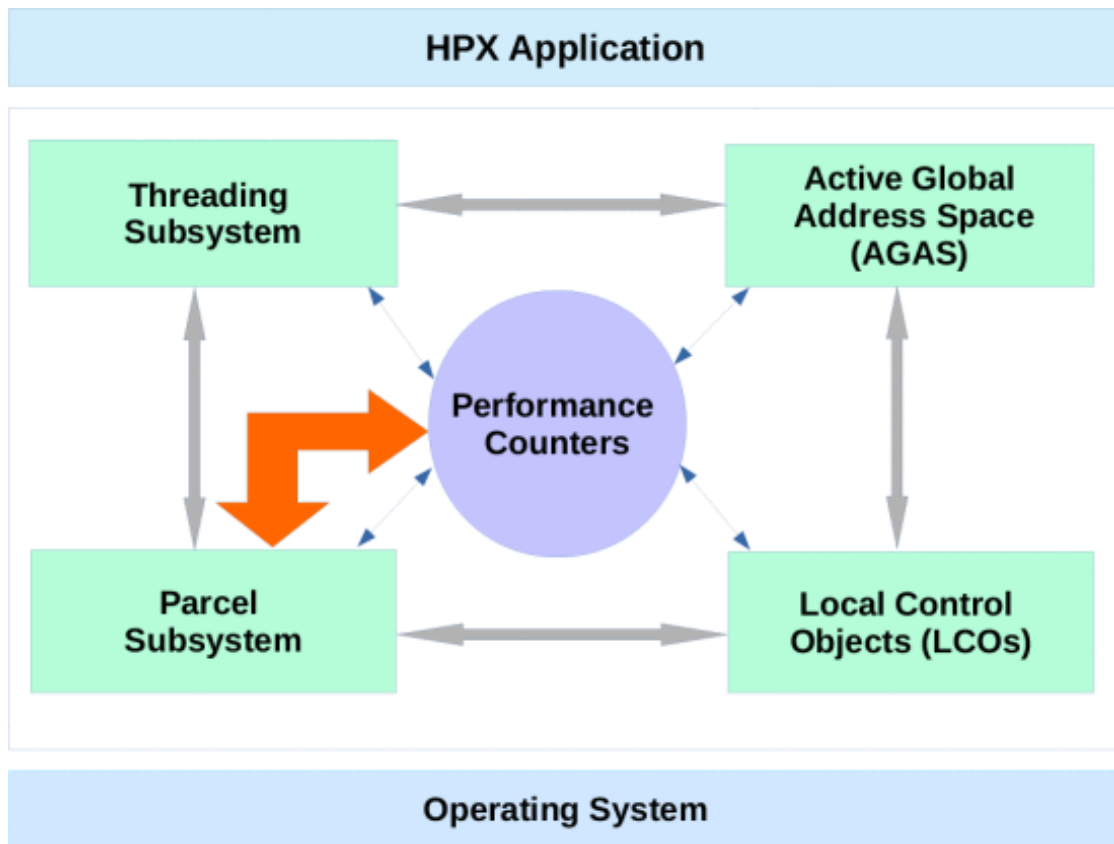


FIGURE 5.3: The underlying architecture of HPX. The architecture of HPX consists of threading subsystem, active global address space (agas), local control objects (lcos) and the parcel subsystem with the performance counter framework interacting with each of the subsystems for instrumentation and debugging purposes.

What follows is a gentle introduction to the parcel subsystem and the Performance Counter Framework of HPX.

A parcel(Parallel Control Element) is a form of an active message [75]. A parcel is created when a method, called action in HPX terminology, is called remotely. The structure of a HPX Parcel is shown in Fig. 5.4. The destination address is the location where the method is to be executed, action is the method to execute, arguments are the parameters of the method and optionally present continuations are work that will be executed after the main method in the parcel terminates. In order to transmit a parcel over the network, a parcel goes through a serialization process converting it into a stream of bytes which is then sent over the wire using

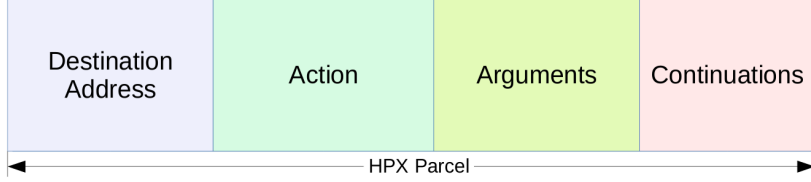


FIGURE 5.4: Structure of an HPX parcel. A parcel has four components: the destination address (the address of the locality where the parcel is destined); the action, which is the method/function to execute at the destination; the arguments for the function; and optional continuations.

existing network protocols. HPX at present supports TCP/IP and is also able to use the MPI communications library for sending sequences of bytes to remote nodes. At the receiving end, a deserialization process reconstructs the parcel from the received sequence of bytes. The parcel is then converted into a HPX thread and placed in the scheduler queue for execution. The parcel subsystem is responsible for creating the parcels as well as converting a received parcel into a HPX thread.

5.5 Application on the Parquet Algorithm

These efforts resulted in a notable speedup of the single site parquet simulation. The parameters controlled by HPX for the network were the wait time and the message size. The wait time determined the amount of time the simulation should wait after receiving the first information to send. The message size served as a maximum size of message to send across the network. Ideally managing these two parameters would minimize network overhead. As shown in Fig. 5.5 the simulation sped up by 30% with the appropriate choice of parameters. The downside to this is that a brute force over the parameter space was required to find the optimal setting each time a new simulation was run.

5.6 Summary

The performance of applications that generate large numbers of small parcels in task based runtime systems such as HPX can be improved by coalescing these small parcels into larger ones. This improvement is largely due to reduction in network

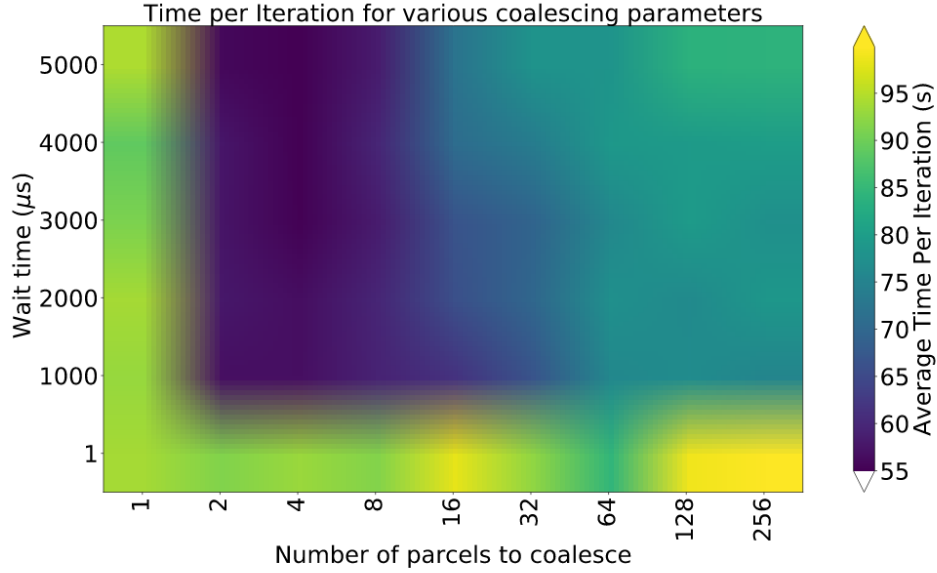


FIGURE 5.5: The network parameters resulting in speedup of parquet simulation. The network parameters of wait time until a packet is sent and size of message to be sent had a significant effect on the speed of the parquet simulation. The correct choice of parameters resulted in a 30% speedup.

overheads as fewer messages are created. However, static approaches towards coalescing parameter selection can only provide limited gains in performance. Adaptive techniques are needed to make further reductions in application execution times. Charm++ [72] has shown the effectiveness of automatic configuration parameter selection using PICS: A Performance-Analysis-Based Introspective Control System [73]. Their approach tested a set of configuration parameters for each iteration of the application and chose new parameters based on the performance measured during that iteration.

This approach to adaptive tuning is only suited for iterative applications, and therefore, this technique is unable to consider the phase of the application. The methodology introduced in this research improves upon the state of the art by introducing new intrinsic performance counters which provide the current state of the application in real time. Using information obtained from such counters, one

can make a distinction between different communication phases of the application and select configuration parameters accordingly.

Metrics identified in this research have shown a strong correlation with execution time of the parquet application. Furthermore, Fig. 9 demonstrated that changing the coalescing parameters at runtime could influence the instantaneous network overhead. This result indicates that data obtained from intrinsic performance counters could be used to make adaptive decisions. This allows for intelligent adaptive behavior where one can employ different configuration settings depending upon the phase of the application.

Chapter 6

Conclusion

6.1 Summary

This work explores the Hubbard model in three dimensions. Specifically it utilizes the DCA in order to analyze the features of the single particle properties at low but non-zero temperature. The low temperatures accessible demonstrate that the Hubbard model enters different phases dependent upon the momentum distribution of the system. This success relies largely on the increased resolution afforded by the cluster approximation.

The cluster allows for the selection of the momentum point closest to the Fermi surface. With a mean field approach, such as the DMFA, the entire Brillouin zone would be mapped to a single point and the resolution would not be sufficient to identify the differences between the different fillings. This allowed the clear identification of a Fermi liquid state and a non-Fermi liquid state.

The different states were identified through an analysis of the single particle self-energy. The quasiparticle weight extracted from the lowest frequency point in the self-energy behaved differently as the system approached half-filling. The quasiparticle weight approached a finite value as the temperature approached zero for $N < 0.95$ indicating a Fermi liquid state. Above this value the quasiparticle weight drops to zero as the temperature approaches zero indicating a non-Fermi liquid state. This transition hints at the possibility of a quantum critical point.

Additionally, the quasiparticle weights in the Fermi liquid state were fit to a crossover form. This crossover form identified the temperature at which the three dimensional Hubbard model left the Marginal Fermi liquid state and crossed over to the Fermi liquid state. The temperature shows a monotonically decreasing trend

from the fit parameters. This serves as an additional indication of the presence of a quantum critical point. This seems to point to a zero temperature crossover temperature at a filling of $N = 0.95$ which matches the data generated.

Finally, there is the emergence of a pseudogap in the system near half filling. This gap emerges as the temperature decreases. It would be expected to coincide with a maximum in the cluster spin susceptibility. This was observed for $N = 0.97$ though the noise in the other fillings was such that it was impossible to identify the exact temperature of the maximum susceptibility. Nonetheless, this is an indication that the non Fermi liquid state is a pseudogap state.

This study shows that there is a transition in the simulations of the three dimensional Hubbard model from a Fermi liquid state to a non-Fermi liquid state. This may be an indicator of a quantum critical point in three dimensions following the same trend seen in the two dimensional Hubbard model. These are not concrete evidences and further study is required in order to definitively determine the existence of a quantum critical point in three dimensions.

6.2 Network Performance

The work in conjunction with HPX gave promising results in the field of network performance. It improved the single iteration time for the parquet step by 30%. This was the result of coalescing the small messages of the parquet step in the simulation and sending them together. This reduced the load on the network and allowed for the simulation to complete more efficiently.

This effort led to the implementation of a parameter within HPX which could be enabled in order to measure the instantaneous network overhead and adjust accordingly. This development is freely available and may be expanded to be automated. As it stands it is a low cost alternative to fine tuning manually using precious developer time to run the simulation efficiently.

6.3 Importance

This work serves to highlight a connection between the two dimensional and three dimensional Hubbard model. Both the two dimensional and the three dimensional models seem to have a quantum critical point away from half-filling.

This could extend beyond the work of the Cuprates. The cuprates are seen as pseudo two dimensional systems. In systems such as cold atoms [76, 77] the interest in the three dimensional Hubbard model is increasing. The possibility to investigate the susceptibility in order to search for an evidence of the emergence of a pseudogap seems promising. Additionally, simply improving this calculation to identify an accurate quantum critical point would be a major success for the Hubbard model. This would indicate the possibility of finding a quantum critical point in a three dimensional strongly correlated system.

6.4 Future Work

The work should be continued by initially improving the accuracy of the calculations themselves. The susceptibility should be of particular note as it currently is a very noisy calculation. With this and a better understanding of where exactly the pseudogap emerges there would be a clear indication of a quantum critical point.

The work should similarly be continued in the avenue of exploring the thermodynamic properties of the system. The thermodynamic properties such as the free energy and entropy should be extractable from the quantities accessible through these simulations though a high precision will be required. Additionally the dynamics of the self-energy and susceptibilities could be explored in detail.

References

- [1] Dimitrios Galanakis, Ehsan Khatami, Karlis Mikelsons, Alexandru Macridin, J Moreno, Dana A Browne, and Mark Jarrell. Quantum criticality and incipient phase separation in the thermodynamic properties of the hubbard model. *Philosophical Transactions of the Royal Society A: Mathematical, Physical and Engineering Sciences*, 369(1941):1670–1686, 2011.
- [2] P. Limelette, A. Georges, D. Jérôme, P. Wzietek, P. Metcalf, and J. M. Honig. Universality and critical behavior at the mott transition. *Science*, 302(5642):89–92, 2003.
- [3] C. G. Shull, W. A. Strauser, and E. O. Wollan. Neutron diffraction by paramagnetic and antiferromagnetic substances. *Phys. Rev.*, 83:333–345, Jul 1951.
- [4] M. Plihal, D. L. Mills, and J. Kirschner. Spin wave signature in the spin polarized electron energy loss spectrum of ultrathin fe films: Theory and experiment. *Phys. Rev. Lett.*, 82:2579–2582, Mar 1999.
- [5] A P Ramirez. Colossal magnetoresistance. *Journal of Physics: Condensed Matter*, 9(39):8171–8199, sep 1997.
- [6] T. Chakraborty and P. Pietiläinen. *The fractional quantum Hall effect: properties of an incompressible quantum fluid*. Springer series in solid-state sciences. Springer, 1988.
- [7] J. G. Bednorz and K. A. Müller. Possible hightc superconductivity in the ba-la-cu-o system. *Zeitschrift für Physik B Condensed Matter*, 64(2):189–193, Jun 1986.
- [8] M. K. Wu, J. R. Ashburn, C. J. Torng, P. H. Hor, R. L. Meng, L. Gao, Z. J. Huang, Y. Q. Wang, and C. W. Chu. Superconductivity at 93 k in a new mixed-phase y-ba-cu-o compound system at ambient pressure. *Phys. Rev. Lett.*, 58:908–910, Mar 1987.
- [9] Ayako Yamamoto, Nao Takeshita, Chieko Terakura, and Yoshinori Tokura. High pressure effects revisited for the cuprate superconductor family with highest critical temperature. *Nature Communications*, 6(1):8990, Dec 2015.
- [10] Jing Xia, Elizabeth Schemm, G. Deutscher, S. A. Kivelson, D. A. Bonn, W. N. Hardy, R. Liang, W. Siemons, G. Koster, M. M. Fejer, and A. Kapitulnik. Polar kerr-effect measurements of the high-temperature $yba_2cu_3o_{6+x}$ superconductor: Evidence for broken symmetry near the pseudogap temperature. *Phys. Rev. Lett.*, 100:127002, Mar 2008.
- [11] B. Fauqué, Y. Sidis, V. Hinkov, S. Pailhès, C. T. Lin, X. Chaud, and P. Bourges. Magnetic order in the pseudogap phase of high- T_C superconductors. *Phys. Rev. Lett.*, 96:197001, May 2006.

- [12] Subir Sachdev. Colloquium: Order and quantum phase transitions in the cuprate superconductors. *Rev. Mod. Phys.*, 75:913–932, Jul 2003.
- [13] AJ Millis. Effect of a nonzero temperature on quantum critical points in itinerant fermion systems. *Physical Review B*, 48(10):7183, 1993.
- [14] C. M. Varma, P. B. Littlewood, S. Schmitt-Rink, E. Abrahams, and A. E. Ruckenstein. Phenomenology of the normal state of cu-o high-temperature superconductors. *Phys. Rev. Lett.*, 63:1996–1999, Oct 1989.
- [15] R. Blankenbecler, D. J. Scalapino, and R. L. Sugar. Monte carlo calculations of coupled boson-fermion systems. i. *Phys. Rev. D*, 24:2278–2286, Oct 1981.
- [16] Steven R. White. Density matrix formulation for quantum renormalization groups. *Phys. Rev. Lett.*, 69:2863–2866, Nov 1992.
- [17] Antoine Georges, Gabriel Kotliar, Werner Krauth, and Marcelo J. Rozenberg. Dynamical mean-field theory of strongly correlated fermion systems and the limit of infinite dimensions. *Rev. Mod. Phys.*, 68:13–125, Jan 1996.
- [18] Kenneth G. Wilson. The renormalization group: Critical phenomena and the kondo problem. *Rev. Mod. Phys.*, 47:773–840, Oct 1975.
- [19] J. E. Hirsch and R. M. Fye. Monte carlo method for magnetic impurities in metals. *Phys. Rev. Lett.*, 56:2521–2524, Jun 1986.
- [20] Charles Kittel. *Introduction to Solid State Physics*. Wiley, 8 edition, 2004.
- [21] H. Ehrenreich and F. Spaepen. *Solid State Physics*. ISSN. Elsevier Science, 2006.
- [22] LD Landau. Zh eksperim. i teor fiz. 30 1058 (1956). *ENGLISH TRANSLATION: Soviet. Phys. JEPT*, 3(920):164, 1956.
- [23] Philip W Anderson. *Basic notions of condensed matter physics*. CRC Press, 2018.
- [24] K. Andres, J. E. Graebner, and H. R. Ott. 4f-virtual-bound-state formation in CeAl_3 at low temperatures. *Phys. Rev. Lett.*, 35:1779–1782, Dec 1975.
- [25] CM Varma, Z Nussinov, and Wim van Saarloos. Singular or non-fermi liquids. *Physics Reports*, 361(5-6):267–417, 2002.
- [26] Alekseĭ Alekseevich Abrikosov, Lev Petrovich Gorkov, and Igor Ekhielevich Dzyaloshinski. *Methods of quantum field theory in statistical physics*. Courier Corporation, 2012.
- [27] Gordon Baym and Christopher Pethick. *Landau Fermi-liquid theory: concepts and applications*. John Wiley & Sons, 2008.

- [28] Rev Shankar. Renormalization-group approach to interacting fermions. *Reviews of Modern Physics*, 66(1):129, 1994.
- [29] Patrick A. Lee, Naoto Nagaosa, and Xiao-Gang Wen. Doping a mott insulator: Physics of high-temperature superconductivity. *Rev. Mod. Phys.*, 78:17–85, Jan 2006.
- [30] J. Bardeen. Theory of the Meissner Effect in Superconductors. *Physical Review*, 97(6):1724–1725, Mar 1955.
- [31] Leon N. Cooper. Bound Electron Pairs in a Degenerate Fermi Gas. *Physical Review*, 104(4):1189–1190, Nov 1956.
- [32] J. Bardeen, L. N. Cooper, and J. R. Schrieffer. Microscopic Theory of Superconductivity. *Physical Review*, 106(1):162–164, Apr 1957.
- [33] J. Bardeen, L. N. Cooper, and J. R. Schrieffer. Theory of Superconductivity. *Physical Review*, 108(5):1175–1204, Dec 1957.
- [34] J.W. Rohlf. *Modern Physics from alpha to Z0*. Wiley, 1994.
- [35] James W. Garland. Isotope effect in superconductivity. *Phys. Rev. Lett.*, 11:114–119, Aug 1963.
- [36] Ivar Giaever and Karl Megerle. Study of superconductors by electron tunneling. *Phys. Rev.*, 122:1101–1111, May 1961.
- [37] M. Tinkham. *Introduction to Superconductivity*. Dover Books on Physics Series. Dover Publications, 2004.
- [38] T. Watanabe, T. Fujii, and A. Matsuda. Anisotropic resistivities of precisely oxygen controlled single-crystal $\text{Bi}_2\text{Sr}_2\text{CaCu}_2\text{O}_{8+\delta}$: Systematic study on “spin gap” effect. *Phys. Rev. Lett.*, 79:2113–2116, Sep 1997.
- [39] Henri Alloul. NMR in correlated electron systems : Illustration on the cuprates. In *Quantum Materials: Experiment and Theory*, chapter 13. Institute for Advanced Simulation, 2016.
- [40] J.L. Tallon, T. Benseman, G.V.M. Williams, and J.W. Loram. The phase diagram of high- T_c superconductors. *Physica C: Superconductivity*, 415(1):9 – 14, 2004.
- [41] John Hubbard. Electron correlations in narrow energy bands. *Proceedings of the Royal Society of London. Series A. Mathematical and Physical Sciences*, 276(1365):238–257, 1963.
- [42] Lev Davidovich Landau. On the theory of phase transitions. *Ukr. J. Phys.*, 11:19–32, 1937.

- [43] John A Hertz. Quantum critical phenomena. *Physical Review B*, 14(3):1165, 1976.
- [44] J. Hubbard and Brian Hilton Flowers. Electron correlations in narrow energy bands iii. an improved solution. *Proceedings of the Royal Society of London. Series A. Mathematical and Physical Sciences*, 281(1386):401–419, 1964.
- [45] W. F. Brinkman and T. M. Rice. Application of gutzwiller’s variational method to the metal-insulator transition. *Phys. Rev. B*, 2:4302–4304, Nov 1970.
- [46] Vladimir V. Uchaikin and Vladimir M. Zolotarev. *Chance and Stability*. De Gruyter, Berlin, Boston, 1999.
- [47] Walter Metzner and Dieter Vollhardt. Correlated lattice fermions in $d = \infty$ dimensions. *Phys. Rev. Lett.*, 62:324–327, Jan 1989.
- [48] Walter Metzner. Variational theory for correlated lattice fermions in high dimensions. *Zeitschrift für Physik B Condensed Matter*, 77:253–266, Jun 1989.
- [49] E. Müller-Hartmann. Correlated fermions on a lattice in high dimensions. *Zeitschrift für Physik B Condensed Matter*, 74:507–512, 12 1989.
- [50] D. B. McWhan and J. P. Remeika. Metal-insulator transition in $(V_{1-x}Cr_x)_2O_3$. *Phys. Rev. B*, 2:3734–3750, Nov 1970.
- [51] D. B. McWhan, A. Menth, J. P. Remeika, W. F. Brinkman, and T. M. Rice. Metal-insulator transitions in pure and doped $v_2 o_3$. *Phys. Rev. B*, 7:1920–1931, Mar 1973.
- [52] T. M. Rice and D. B. McWhan. Metal-insulator transition in transition metal oxides. *IBM Journal of Research and Development*, 14(3):251–257, 1970.
- [53] Antoine Georges, Gabriel Kotliar, Werner Krauth, and Marcelo J. Rozenberg. Dynamical mean-field theory of strongly correlated fermion systems and the limit of infinite dimensions. *Rev. Mod. Phys.*, 68:13–125, Jan 1996.
- [54] Emanuel Gull, Andrew J. Millis, Alexander I. Lichtenstein, Alexey N. Rubtsov, Matthias Troyer, and Philipp Werner. Continuous-time monte carlo methods for quantum impurity models. *Rev. Mod. Phys.*, 83:349–404, May 2011.
- [55] Herbert Fotso. *Two-particle level diagrammatic approaches for strongly correlated systems*. PhD thesis, 2011.
- [56] N. S. Vidhyadhiraja, A. Macridin, C. Şen, M. Jarrell, and Michael Ma. Quantum critical point at finite doping in the 2d hubbard model: A dynamical cluster quantum monte carlo study. *Phys. Rev. Lett.*, 102:206407, May 2009.

- [57] H. Terletska, J. Vučičević, D. Tanasković, and V. Dobrosavljević. Quantum critical transport near the mott transition. *Phys. Rev. Lett.*, 107:026401, Jul 2011.
- [58] D.W. Hess and J.W. Serene. Self consistent numerical calculations for nested fermi liquids. *Journal of Physics and Chemistry of Solids*, 52(11):1385 – 1390, 1991.
- [59] D D Betts and G E Stewart. Estimation of zero-temperature properties of quantum spin systems on the simple cubic lattice via exact diagonalization on finite lattices. *Canadian Journal of Physics*, 75(1):47–66, 1997.
- [60] Donald Shepard. A two-dimensional interpolation function for irregularly-spaced data. In *Proceedings of the 1968 23rd ACM National Conference*, ACM '68, page 517–524, New York, NY, USA, 1968. Association for Computing Machinery.
- [61] B. Wagle, S. Kellar, A. Serio, and H. Kaiser. Methodology for adaptive active message coalescing in task based runtime systems. In *2018 IEEE International Parallel and Distributed Processing Symposium Workshops (IPDPSW)*, pages 1133–1140, 2018.
- [62] Cyrano De Dominicis and Paul C. Martin. Stationary entropy principle and renormalization in normal and superfluid systems. ii. diagrammatic formulation. *Journal of Mathematical Physics*, 5(1):31–59, 1964.
- [63] Hartmut Kaiser, Thomas Heller, Bryce Adelstein-Lelbach, Adrian Serio, and Dietmar Fey. Hpx: A task based programming model in a global address space. In *Proceedings of the 8th International Conference on Partitioned Global Address Space Programming Models*, pages 1–11, 2014.
- [64] B. Roulet, J. Gavoret, and P. Nozières. Singularities in the x-ray absorption and emission of metals. i. first-order parquet calculation. *Phys. Rev.*, 178:1072–1083, Feb 1969.
- [65] Victor M. Yakovenko. Metals in a high magnetic field: A universality class of marginal fermi liquids. *Phys. Rev. B*, 47:8851–8857, Apr 1993.
- [66] P. Kleinert and H. Schlegel. Parquet approximation for a disordered two-dimensional electron gas in a strong transverse magnetic field. *Physica A: Statistical Mechanics and its Applications*, 218(3):507 – 525, 1995.
- [67] William Gropp, Ewing Lusk, Nathan Doss, and Anthony Skjellum. A high-performance, portable implementation of the mpi message passing interface standard. *Parallel computing*, 22(6):789–828, 1996.
- [68] Richard P Martin, Amin M Vahdat, David E Culler, and Thomas E Anderson. Effects of communication latency, overhead, and bandwidth in a cluster architecture. *ACM SIGARCH Computer Architecture News*, 25(2):85–97, 1997.

- [69] Cong-Duc Pham. Comparison of message aggregation strategies for parallel simulations on a high performance cluster. In *Proceedings 8th International Symposium on Modeling, Analysis and Simulation of Computer and Telecommunication Systems (Cat. No. PR00728)*, pages 358–365. IEEE, 2000.
- [70] Jeremiah James Willcock, Torsten Hoefler, Nicholas Gerard Edmonds, and Andrew Lumsdaine. Active pebbles: parallel programming for data-driven applications. In *Proceedings of the international conference on Supercomputing*, pages 235–244, 2011.
- [71] Jeremiah J Willcock, Torsten Hoefler, Nicholas G Edmonds, and Andrew Lumsdaine. Am++: A generalized active message framework. In *2010 19th International Conference on Parallel Architectures and Compilation Techniques (PACT)*, pages 401–410. IEEE, 2010.
- [72] Lukasz Wesolowski, Ramprasad Venkataraman, Abhishek Gupta, Jae-Seung Yeom, Keith Bisset, Yanhua Sun, Pritish Jetley, Thomas R Quinn, and Laxmikant V Kale. Tram: Optimizing fine-grained communication with topological routing and aggregation of messages. In *2014 43rd International Conference on Parallel Processing*, pages 211–220. IEEE, 2014.
- [73] Yanhua Sun, Jonathan Lifflander, and Laxmikant V Kalé. Pics: a performance-analysis-based introspective control system to steer parallel applications. In *Proceedings of the 4th International Workshop on Runtime and Operating Systems for Supercomputers*, pages 1–8, 2014.
- [74] Hartmut Kaiser, Maciek Brodowicz, and Thomas Sterling. Parallelex an advanced parallel execution model for scaling-impaired applications. In *2009 International Conference on Parallel Processing Workshops*, pages 394–401. IEEE, 2009.
- [75] Thorsten Von Eicken, David E Culler, Seth Copen Goldstein, and Klaus Erik Schausser. Active messages: a mechanism for integrated communication and computation. *ACM SIGARCH Computer Architecture News*, 20(2):256–266, 1992.
- [76] Duarte Pedro M. Hart, Russell A., Tsung-Lin Yang, Xinxing Liu, Thereza Paiva, Ehsan Khatami, Richard T. Scalettar, Nandini Trivedi, David A. Huse, and Randall G. Hulet. Observation of antiferromagnetic correlations in the hubbard model with ultracold atoms. *Nature*, 519(7542):211–214, Mar 2015.
- [77] Jakub Imriška, Mauro Iazzi, Lei Wang, Emanuel Gull, Daniel Greif, Thomas Uehlinger, Gregor Jotzu, Leticia Tarruell, Tilman Esslinger, and Matthias Troyer. Thermodynamics and magnetic properties of the anisotropic 3d hubbard model. *Phys. Rev. Lett.*, 112:115301, Mar 2014.

Vita

Samuel Kellar began his study in physics at Brigham Young University the summer of 2004. He served a religious mission for two years from 2005-2007 postponing his studies during that time. He received a Bachelors of Science in December 2011. He briefly worked as a web developer before beginning his doctoral studies in the field of physics at Louisiana State University in the fall of 2012.